Chemical Engineering Journal 529 (2026) 173140



Contents lists available at ScienceDirect

Chemical Engineering Journal

journal homepage: www.elsevier.com/locate/cej



Single-tube total analysis system for ratiometric detection of exosomal miRNAs in breast cancer diagnosis

Myeong-Jun Lee [a], Jeong-Hyeop Shin [a], Seung-Hun Jung [a], Ha Rim Ahn [b], Young Jo Kim [c], Jeong-Woo Choi [a], Jin-Ha Choi [d,*], Byung-Keun Oh [a,*]

[a] Department of Chemical and Biomolecular Engineering, Sogang University, Seoul, 04107, Republic of Korea
[b] Department of Surgery, Jeonbuk National University Medical School, Jeonju-si, 54907, Republic of Korea
[c] Department of Chemical Engineering & Bioengineering, University of New Hampshire, Durham, NH, 03824, United States
[d] School of Chemical Engineering, Jeonbuk National University, Jeonju-si, 54896, Republic of Korea

ARTICLE INFO

Keywords:
Exosome
miRNA
Single-tube
Isothermal amplification
Total analysis system
Breast cancer

ABSTRACT

Although exosomal microRNAs (Exo-miRs) show great promise as stable and disease-specific biomarkers for early cancer detection, current detection workflows remain technically fragmented into multiple discrete steps (exosome isolation, miRNA amplification, and signal detection), requiring inter-step sample transfers. In addition, most existing platforms lack effective normalization strategies, hindering accurate cancer diagnosis because of intersample variation in exosome yield. Here, we developed a single-tube Exo-miRs total analysis system (ST-Exo-TAS) that integrates the entire Exo-miR workflow within a single reaction tube, enabling normalized analysis of target Exo-miRs. The system employs promoter-enriched gold nanoparticles conjugated with anti-CD63 antibodies (Pr/CD63Ab/AuNPs), which serve a dual function: isolating exosomes via immunoaffinity under low-speed centrifugation (6000 *g*, 10 min) and acting as promoter scaffolds for one-pot isothermal elongation and amplification (OPIEA). Following isolation, the captured Exo-miRs are directly subjected to OPIEA at 37 °C using SplintR ligase and T7 polymerase, generating light-up aptamers templated by miR-21 (target) and miR-U6 (internal control). This enables ratiometric dual-fluorescence detection via simple dye addition. ST-Exo-TAS demonstrated high sensitivity, with limits of detection of 1.179 fM for miR-21 and 843.9 aM for miR-U6, and high specificity within a short assay time (sample-to-answer = 150 min). Furthermore, the system was validated using preclinical and clinical samples. Breast cancer cases were successfully distinguished by quantifying Exo-miR-21 expression normalized to that of miR-U6, which helped minimize intersample variation in exosome yield (AUC = 1). This rapid, compact, and user-friendly platform offers a powerful tool for early breast cancer diagnosis and holds strong potential in point-of-care diagnosis technology.

1. Introduction

Early and accurate disease diagnosis is essential for improving treatment outcomes and patient survival [1,2]. In recent years, exosomes, which are nanosized extracellular vesicles released by cells, have attracted significant attention because of their critical roles in intercellular communication and disease progression [3]. Importantly, exosomes carry a variety of biomolecular cargos, including proteins, DNA, and RNA, that reflect the physiological state of their originating cells [4]. Among these, exosomal microRNAs (Exo-miRs) are particularly promising biomarkers because of their stability in body fluids, resistance to enzymatic degradation, and ability to modulate gene expression and biological processes [5].

Despite their clinical potential, conventional analytical workflows remain fragmented and technically demanding in daily clinical use. These workflows typically involve multiple discrete steps, including exosome isolation or enrichment, RNA purification, amplification, and signal detection [6–9]. Each step often requires separate instruments, reagents, and manual handling, contributing to procedural complexity [10,11]. Moreover, this modular configuration prolongs the assay time, increases the risk of sample contamination during transfers, and introduces user- and laboratory-dependent variability, making automation or point-of-care implementation difficult [12,13]. Recent studies have proposed platforms that integrate subsets of the Exo-miR analysis

* Corresponding authors.
E-mail addresses: jhchoi@jbnu.ac.kr (J.-H. Choi), bkoh@sogang.ac.kr (B.-K. Oh).

https://doi.org/10.1016/j.cej.2026.173140
Received 15 October 2025; Received in revised form 23 December 2025; Accepted 16 January 2026
Available online 16 January 2026
1385-8947/© 2026 Elsevier B.V. All rights are reserved, including those for text and data mining, AI training, and similar technologies.

workflow [14,15]. Some systems combine exosome isolation with downstream detection modules, allowing for direct analysis of Exo-miRs without extensive purification [16–18]. Others integrate amplification and signal readout in a single reaction setup, enabling target-specific Exo-miR detection with simplified protocols [19–25]. While these approaches represent meaningful progress toward miniaturized diagnostics, they typically address only isolated segments of the total workflow and still require intermediate steps or sample transfers and often suffer from limited sensitivity. Alternatively, more complex microfluidic systems have been developed to implement fluidically controlled stepwise integration using components such as valves, pumps, and multilayered channel networks. Although these platforms demonstrate the feasibility of integrated Exo-miR analysis, they often depend on external actuation and sophisticated fabrication processes, which limit their scalability and clinical applicability [26–28]. Despite these efforts, a simple and fully integrated system to perform exosome capture, amplification, and detection together in one continuous process has yet to be developed.

However, even with such integration, there is another critical bottleneck in the quantification of exosomal biomarkers. When a target Exo-miR is detected, variations in exosome yield across samples result in substantial fluctuations in signal output, which are caused by both biological heterogeneity and technical inconsistencies [29]. Without an effective normalization strategy, these variations risk obscuring true biological differences and may lead to inaccurate or misleading diagnostic interpretations [30,31]. Nevertheless, most existing platforms do not support the simultaneous detection of target and reference Exo-miRs within the same reaction, making it difficult to control for sample-to-sample variability [32–35]. This limitation is particularly consequential in cancer diagnostics, where analytical consistency is essential for clinical decision-making.

To overcome these limitations, we developed a single-tube exosomal miRNA total analysis system (ST-Exo-TAS), a fully integrated diagnostic platform operating within a single reaction tube for streamlined and normalized Exo-miR detection. Our strategy focuses on two key technologies: (i) a nanomaterial-based total analysis system that enables sequential execution of exosome isolation, ligation-mediated isothermal amplification, and fluorescence detection within a single tube and (ii) a dual-target detection mechanism for intrasample normalization. (i) ST-Exo-TAS employs promoter-enriched gold nanoparticles conjugated with anti-CD63 antibodies (Pr/CD63Ab/AuNPs), which enable selective immunoaffinity-based capture of exosomes under low-speed centrifugation and simultaneously provide a transcriptionally active scaffold for downstream signal amplification. The captured Exo-miRs are then subjected to a one-pot isothermal elongation and amplification (OPIEA) strategy, which ligates the target Exo-miRs, transcribes them using T7 RNA polymerase, and generates a fluorescence signal via light-up aptamers. This approach eliminates the need for RNA elongation, reverse transcription, and thermal cycling, thereby simplifying the workflow without compromising sensitivity. For (ii), the system performs simultaneous detection of Exo-miR-21 (breast cancer diagnosis target) and Exo-miR-U6 (widely used as internal control) using orthogonal light-up aptamers (‘peach’ and ‘broccoli’), enabling real-time normalization and minimizing intersample variability [36–41]. This ratiometric analysis enhances the accuracy and reliability of Exo-miR quantification, particularly in clinical samples where exosome yield may vary. The ST-Exo-TAS introduced in this study is a fully integrated single-tube platform that combines immunoaffinity-based exosome isolation, ligation-mediated isothermal amplification, and dual-aptamer fluorescence detection within a single reaction environment. Unlike conventional systems with physically separated modules, ST-Exo-TAS directly links target capture with signal amplification through a functionalized nanomaterial. This streamlined yet precise workflow offers strong potential for clinical diagnostics and decentralized point-of-care applications.

2. Results and discussion

2.1. Workflow of ST-Exo-TAS

To enable rapid, simplified, and contamination-free detection of cancer-derived Exo-miRs, we developed a fully integrated single-tube platform (ST-Exo-TAS) that seamlessly combines exosome isolation/enrichment, Exo-miR extraction, isothermal amplification, and dual-signal detection in a single-tube workflow. The system's operation is illustrated in Fig. 1A. In brief, plasma samples collected from breast cancer patients are incubated with Pr/CD63Ab/AuNPs for immunoaffinity-based exosome capture (30 min). Following low-speed centrifugation to isolate the exosome–nanoparticle complexes (10 min), all subsequent steps—including exosome lysis (10 min), isothermal amplification of Exo-miRs (90 min), and dual-fluorescence detection (10 min)—are performed sequentially within the reaction tube by stepwise addition of reagents. This overall workflow mimics a fed-batch reaction scheme that does not require the removal of solution. This one-pot workflow is enabled by the integrated design of the Pr/CD63Ab/AuNPs and OPIEA, eliminating the need for tube transfers or intermediate purification steps. In detail, the ST-Exo-TAS operation consists of four major functional stages (Fig. 1B–E). The first step, “Immunoaffinity-based exosome isolation/enrichment using Pr/CD63Ab/AuNPs”, involves selective exosome capture directly from biological fluids, such as plasma or conditioned media, as shown in Fig. 1B. The gold nanoparticles (AuNPs) are functionalized with anti-CD63 antibodies and thiolated promoter sequences (Pr/CD63Ab/AuNPs), imparting dual functionality: (1) immunoaffinity pulldown of CD63-positive exosomes and (2) provision of surface-bound promoter sequences for downstream ligation and transcription-based amplification [42,43]. Upon incubation, Pr/CD63Ab/AuNPs selectively bind to exosomes via CD63 antibody recognition. Owing to the increased mass of the exosome–nanoprobe complex, these can be isolated efficiently via low-speed centrifugation without ultracentrifugation. The resulting pellet contains intact, highly concentrated exosomes suitable for direct downstream analysis. Following exosome isolation/enrichment, Exo-miRs are directly extracted and amplified in the same tube without any sample transfer. As illustrated in Fig. 1C, mild lysis is performed using Triton X-100 to release Exo-miRs into the solution by exosome lysis. Following the reaction, OPIEA solution, which contains target-specific binding ssDNA fragments, SplintR ligase, and T7 polymerase, is added to initiate the OPIEA reaction, as illustrated in Fig. 1D. The extracted target Exo-miRs (targets: Exo-miR-21 and Exo-miR-U6) serve as templates for a ligation-based isothermal amplification reaction by OPIEA. Target-specific DNA probes hybridize to the target Exo-miR, allowing for SplintR ligase to ligate the adjacent probes, forming a transcription template that includes a T7 promoter sequence. With the Pr/CD63Ab/AuNP, T7 RNA polymerase then transcribes the ligated DNA into RNA molecules that encode light-up aptamers specific to each target (Exo-miR-21 to the peach aptamer RNA sequence and Exo-miR-U6 to the broccoli RNA sequence) [44]. Importantly, the transcribed RNA aptamers generated by T7 RNA polymerase retain the original target miRNA sequence. These RNA transcripts can subsequently hybridize with additional DNA probes, acting as secondary splints to facilitate further ligation events. This target-dependent, recursive ligation–transcription process establishes a positive feedback loop, leading to the accumulation of elongated transcription templates beyond the initial ligation step. As a result, signal amplification is achieved without thermal cycling, thereby enhancing both the efficiency and sensitivity of the OPIEA reaction while maintaining strict target specificity. This OPIEA reaction occurs at 37 °C and bypasses conventional steps such as poly-A tailing, reverse transcription, and multienzyme cycling, significantly reducing both the complexity and the risk of contamination. The final step is dual-color fluorescence detection via aptamer–fluorogenic dye complexes by simply adding fluorogenic dyes to the reaction tube. The transcribed RNA aptamers fold into secondary structures capable of

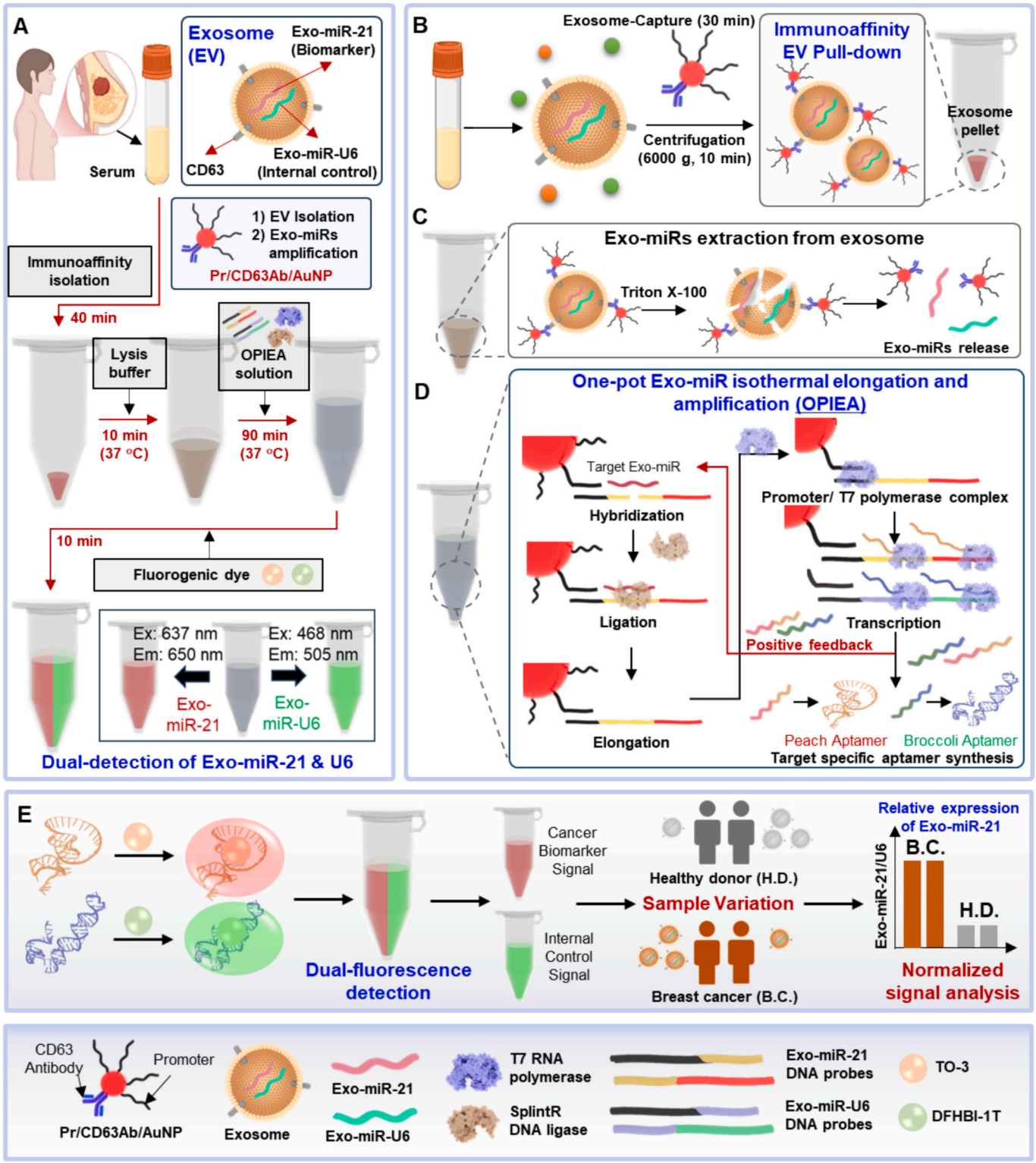


Fig. 1. (A) Schematic illustration of the workflow of the ST-Exo-TAS. (B) Schematic diagram illustrating the isolation of Pr/CD63Ab/AuNP-based immunoaffinity exosomes from samples. (C) Schematic overview of single-tube Exo-miR extraction. (D) Schematic illustration of OPIEA in ST-Exo-TAS. Exo-miR-21 and Exo-miR-U6 hybridize with designed DNA probes to form elongated templates on Pr/CD63Ab/AuNPs, enabling splint ligation and T7-driven transcription into target-encoded RNA light-up aptamers. The transcribed RNA can further act as a secondary splint, establishing a target-dependent positive feedback loop that promotes recursive ligation and amplification. (E) Schematic illustration of the dual detection of amplified RNA aptamers for normalization of sample variation. The amplified product exhibits a fluorescent signal upon binding to the fluorescent dye, a peach aptamer from Exo-miR-21 with TO-3 fluorescent dye (red), and a broccoli aptamer from Exo-miR-U6 with DFHBI-1 T fluorescent dye (green). (For interpretation of the references to color in this figure legend, the reader is referred to the web version of this article.)

binding specific fluorogenic dyes to generate distinct fluorescence signals. For Exo-miR-21 detection, the synthesized RNA forms a peach aptamer, which binds to TO-3 dye and emits red fluorescence (Ex: 637 nm/Em: 650 nm). With respect to Exo-miR-U6, the amplified RNA forms a broccoli aptamer, which binds to DFHBI-1 T and emits green fluorescence (Ex: 468 nm/Em: 505 nm). These orthogonal, nonoverlapping readouts allow for the simultaneous quantification of both Exo-miRs in a single reaction tube, with miR-U6 serving as a robust internal control for normalization (Fig. 1E). By normalizing the Exo-miR-21 signal to the internal reference miR-U6, ST-Exo-TAS enables accurate

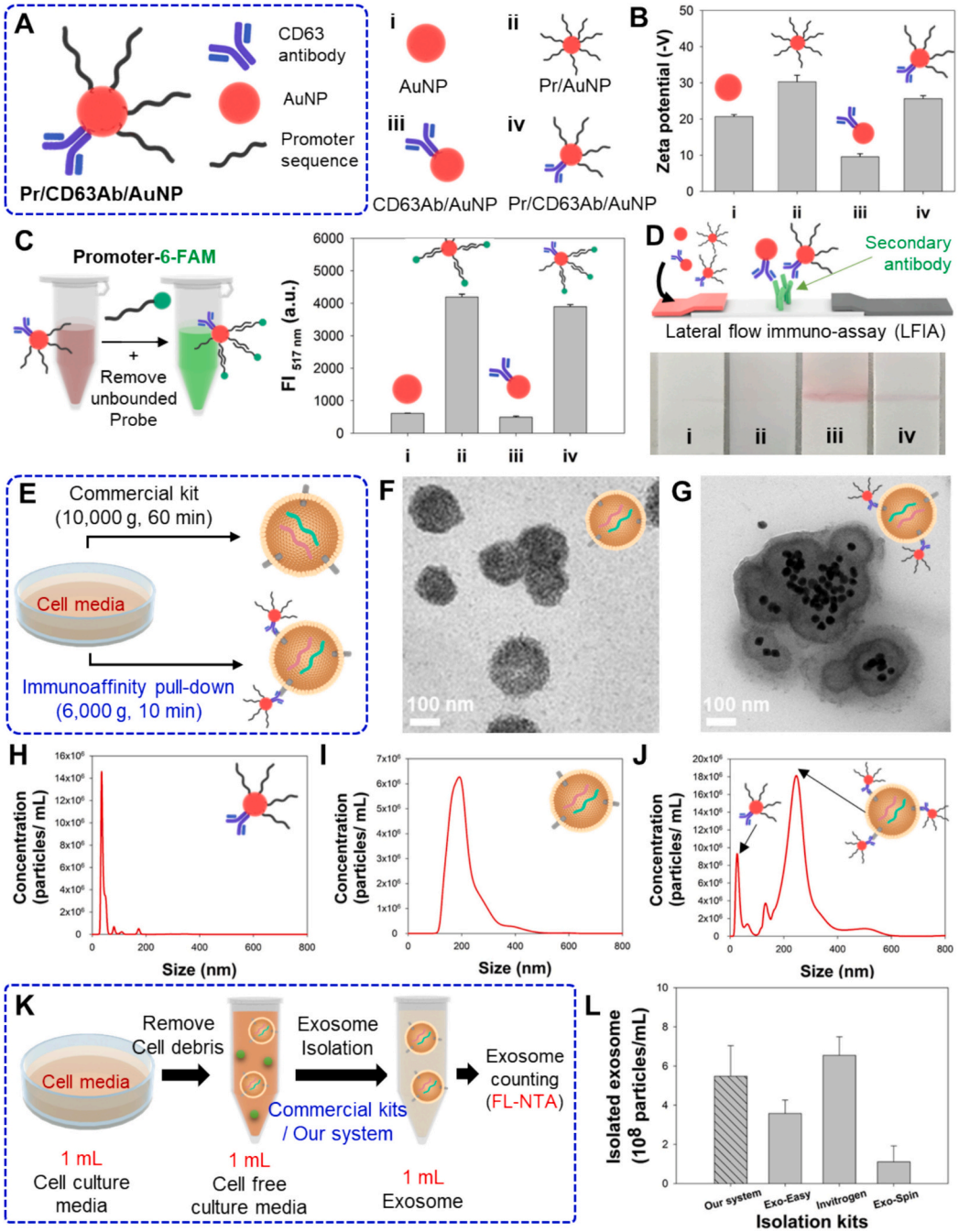


Fig. 2. (A) Schematic illustration of the construction of Pr/CD63Ab/AuNPs and prepared nanoprobes (i) AuNPs, (ii) Pr/AuNP, (iii) CD63Ab/AuNP, and (iv) Pr/CD63Ab/AuNPs for comparison. (B) Surface charge (zeta potential) of the nanoprobes. (C) Schematic illustration of the experimental workflow for confirming the immobilization of the thiolated promoter sequence on the nanoprobes by the 6-Fam-tagged promoter complementary sequence. The fluorescence intensity after the unbound 6-Fam-tagged promoter complementary sequence was removed revealed the successful immobilization of the promoter sequence in the Pr/CD63Ab/AuNPs. (D) Lateral flow immunoassay for confirmation of antibody immobilization on AuNPs by secondary antibody and CD63Ab immunoaffinity. (E) Experimental workflow for the confirmation of exosome isolation from cell media using Pr/CD63Ab/AuNPs. (F) TEM images of exosomes isolated by a commercial kit and (G) Pr/CD63Ab/AuNPs (scale bar = 100 nm). Nanoparticle tracking analysis (NTA) for the size characteristics of (H) Pr/CD63Ab/AuNPs, (I) exosomes isolated by commercial kits, and (J) exosomes isolated from Pr/CD63Ab/AuNPs. The graph shows the average value of repeated NTA of each sample (n = 3). (K) Schematic illustration of the workflow for comparing the number of exosomes isolated using commercial exosome isolation kits versus Pr/CD63Ab/AuNPs from identical MCF-7 cell culture media. (L) Quantification of isolated exosomes analyzed by fluorescence-based nanoparticle tracking analysis (FL-NTA). The graph shows the average values from repeated FL–NTA measurements for each sample (n = 3).

breast cancer diagnosis by compensating for sample-to-sample variability in exosome yield and RNA content.

2.2. Isolation/enrichment of exosomes using Pr/CD63Ab/AuNPs and their characteristics

To achieve efficient immunoaffinity pulldown-based exosome isolation and serve as a functional amplification platform, Pr/CD63Ab/AuNPs were engineered with dual functionality: immunoaffinity-based capture of human exosomes and the provision of single-stranded promoter sequences for one-pot isothermal elongation and amplification of Exo-miRs (Fig. 2A). In this construction, anti-CD63 antibodies were immobilized on AuNPs via physical adsorption, while thiol-modified promoter-aptamer DNA sequences were conjugated through strong thiol–gold interactions. To validate the fabrication of Pr/CD63Ab/AuNPs, we designed and compared the characteristics of four different types of nanoprobes: (i) AuNPs, (ii) Pr/AuNP (without CD63Ab), (iii) CD63Ab/AuNP (without a promoter sequence), and (iv) Pr/CD63Ab/AuNPs. First, we investigated how the conjugation of the antibody and thiol-promoter sequence affects the surface charge of the AuNPs (Fig. 2B). Zeta potential measurements were performed using an SZ-100 nanoparticle analyzer (Horiba, Japan), and the changes in the surface charge of the four types of nanoprobes were measured at pH 7. The results showed that the thiol-promoter sequence with AuNPs (-30.3 ± 1.80 mV) led to an increase in the negative surface charge of the AuNPs (-20.7 ± 0.89 mV) because the ssDNA had a negative charge. On the other hand, the conjugation of the anti-CD63 antibody with the AuNPs resulted in a decreased negative charge (-9.63 ± 0.78 mV) compared to that of the AuNPs because the antibody was less negatively charged than the AuNPs were. On the basis of these results, we can assume that the negative charge of the Pr/CD63Ab/AuNP was greater than that of the CD63Ab/AuNP but lower than that of the Pr/AuNP. The surface charge of the Pr/CD63Ab/AuNP was -25.7 ± 0.78 mV, indicating that it is characteristic of Pr/AuNP and CD63Ab/AuNP. To confirm the binding of the thiol-promoter sequence with the AuNPs in more detail, 4 types of nanoprobes (AuNP, Pr/AuNP, CD63Ab/AuNP, and Pr/CD63Ab/AuNP) were incubated with 6-carboxyfluorescein (6-FAM)-labeled ssDNA sequences complementary to the promoter region (Fig. 2C). After the unbound oligonucleotides were removed, fluorescence measurements revealed a significant signal only in the promoter sequence-conjugated nanoprobe (Pr/AuNP, Pr/CD63Ab/AuNP), confirming sequence-specific hybridization and successful conjugation of the promoter.

Next, the presence of anti-CD63 antibodies on the nanoprobe surface was verified. To confirm antibody immobilization on the AuNPs, a lateral flow immunoassay (LFIA) was performed using a secondary antibody immobilized on a nitrocellulose membrane that could capture the antibody on the nanoprobe (Fig. 2D). When applied to the LFIA strip, antibody-conjugated nanoprobes (CD63Ab/AuNP and Pr/CD63Ab/AuNP) generated a clear red signal, whereas AuNPs and Pr/AuNP did not, confirming antibody immobilization in Pr/CD63Ab/AuNP. In addition, the UV–Vis absorption spectra revealed a distinct peak at approximately 200 nm for Pr/CD63Ab/AuNPs, which is indicative of the peptide residues in the conjugated antibodies, whereas this peak was absent in Pr/AuNPs lacking the antibody component (Fig. S1). Furthermore, a redshift in the surface plasmon resonance (SPR) peak was observed upon antibody conjugation, further confirming successful bioconjugation to the nanoparticle surface. We also conducted gel electrophoresis of 4 types of nanoprobes with a fluorescent (Alexa 488)-conjugated secondary antibody to visualize the anti-CD63 antibodies on the nanoprobe (Fig. S2). As a result, only the antibody-conjugated nanoprobe band showed a fluorescence signal because of the interaction between the antibody and the fluorescently labeled secondary antibody. In addition, transmission electron microscopy (TEM) analysis of the Pr/CD63Ab/AuNPs revealed a distinct core–shell morphology, in which a peripheral layer corresponding to the protein/DNA corona surrounding the gold nanoparticle (AuNP) core was observed. This shell-like structure indicates the successful immobilization of both protein and DNA moieties onto the AuNP surface, confirming the formation of a stable biomolecular corona (Fig. S3). These results also indicated that the Pr/CD63Ab/AuNP was well-fabricated. For quantitative characterization analysis of the Pr/CD63Ab/AuNPs nanoprobes, we performed a detailed analysis to determine the average number of DNA strands and antibodies conjugated per AuNP. As a result, we calculated that approximately 58 antibodies and 322 ssDNA strands were conjugated to each Pr/CD63Ab/AuNP (Table S1). Notably, this conjugation densities fall well within the range reported in previous studies, where 30 nm AuNPs have been shown to accommodate on the order of 100–145 antibodies and 300–600 DNA strands per particle, depending on surface chemistry and conjugation strategy [45–47]. This consistency with established literature supports the rationality and reproducibility of the nanoprobe fabrication process.

After confirming the structural integrity of the Pr/CD63Ab/AuNP, we evaluated the exosome isolation capability of the Pr/CD63Ab/AuNP. First, the isolation ability of the exosomes was investigated. The workflow, illustrated in Fig. 2E, involved direct incubation of Pr/CD63Ab/AuNPs with conditioned media, followed by low-speed centrifugation (6000 *g*, 10 min) to pellet the exosome–nanoprobe complexes. As a control test, exosomes were isolated by commercial kits. First, the isolated exosomes were analyzed using TEM. TEM revealed that the morphology of the exosomes isolated by commercial kits generally ranged from 50 to 200 nm (Fig. 2F). Similarly, the morphology of the exosomes isolated by Pr/CD63Ab/AuNP was comparable to that of those isolated using a commercial kit with vesicular structures (Fig. 2G). In addition, the Pr/CD63Ab/AuNPs are attached to the exosome surface, and it was confirmed that they can separate from the exosome without damage, as with the existing commercial kit.

Nanoparticle tracking analysis (NTA) was performed to characterize the size distribution of the nanoprobes and to evaluate the formation of nanoparticle–exosome complexes. The average hydrodynamic diameter of bare Pr/CD63Ab/AuNPs was approximately 38 nm, which is consistent with the expected size of the functionalized gold nanoparticles (Fig. 2H). Exosomes isolated using a commercial kit exhibited a typical size distribution centered at approximately 200 nm, in line with previously reported values for exosomes derived from human cells (Fig. 2I). In contrast, when the exosomes were isolated using Pr/CD63Ab/AuNPs, the measured size distribution showed a distinct peak at approximately 250 nm (Fig. 2J). This increase in hydrodynamic diameter strongly suggests the formation of exosome–nanoparticle complexes via specific antibody–antigen interactions between the anti-CD63 antibody and CD63 molecules expressed on the exosomal membrane. The larger effective particle size and increased mass of the complex enabled efficient isolation by low-speed centrifugation (6000 *g*), in contrast to the high centrifugal forces (>100,000 *g*) typically required for conventional exosome isolation. Furthermore, to compare the efficiency of exosome isolation by our system and commercial kits, the concentration of exosomes isolated from 1 mL of cell culture media was measured and compared by fluorescence-based nanoparticle tracking analysis (FL-NTA) for selectively counting exosomes (Fig. 2K). The selection kits used were an Exo-Easy (QIAGEN), a total exosome isolation kit (Invitrogen), and an Exo-spin (Cell Guidance System), which are widely used in exosome research (Table S2). Through comparisons with other kits, we confirmed that our system showed a similar exosome separation performance to that of the other kits (Fig. 2L). However, compared with conventional kits, our system has several advantages, such as a lower centrifugation speed, shorter time, and lower cost. Furthermore, unlike other kits, our isolation system will allow for isolation of only human cell-derived exosomes and not all exosomes, helping to reduce nonspecific occurrences in experiments.

2.3. Investigation and confirmation of OPIEA for target Exo-miR amplification

To validate the working mechanism of the OPIEA system, we conducted a series of experiments to confirm each step of the reaction cascade, from target miR-guided probe ligation to RNA aptamer synthesis and light-up fluorescence detection. As illustrated in Fig. 3A, the OPIEA system operates via SplintR ligase–mediated ligation of a pair of DNA probes that hybridize to adjacent sites of the target miRs (miR-21 or miR-U6). The ligated product serves as a transcription template, which includes a T7 promoter region and an aptamer-encoding domain. To confirm this ligation step, agarose gel electrophoresis was performed under various reaction conditions (Fig. 3B). A distinct band corresponding to the elongated template was observed only when miR-21, SplintR ligase, and 37 °C incubation were simultaneously applied (Lane 2). No ligation occurred under control conditions lacking the ligase (Lane 3), target miR-21 (Lane 4), or proper temperature (Lane 5), confirming the specificity and thermally driven enzymatic activity of the ligation process. Next, we evaluated the quantitative correlation of the ligation reaction by titrating target miR-21 from 100 nM down to 0.1 nM. As shown in Fig. 3C, the band intensity of the elongated product increased proportionally with increasing target miR-21 concentration, indicating that ligation efficiency directly reflects target abundance. Following ligation analysis, the ligation-transcription-based OPIEA was

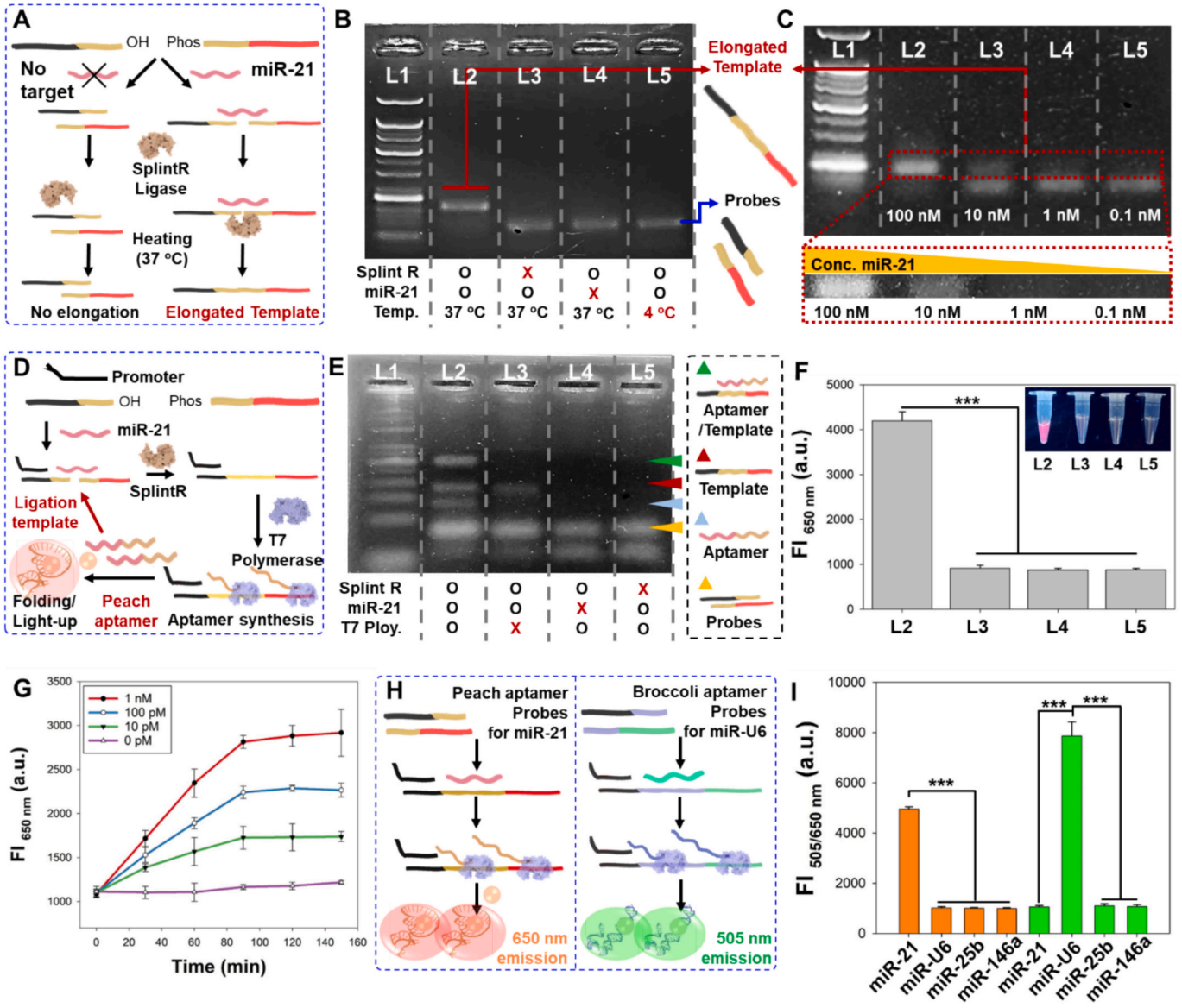


Fig. 3. (A) Schematic illustration of SplintR ligase-based elongation of DNA probes using miR-21 (Phos: phosphorylated, OH: hydroxyl group). (B) Agarose gel electrophoresis image of the ligation process using miR-21 and SplintR ligase (L1: DNA size marker; probe pair mixed with L2: SplintR ligase at 37 °C; L3: L2 without SplintR ligase; L4: L2 without miR-21; L5: L2 at 4 °C). (C) Agarose gel electrophoresis image of the ligation results according to the concentration of miR-21 (L1: DNA size marker; L2: 100 nM; L3: 10 nM, L4: 1 nM, L5 0.1 nM of miR-21). (D) Schematic illustration of the OPIEA system for miR-21 amplification to the peach aptamer. (E) Agarose gel electrophoresis image of the OPIEA system at 37 °C (L1: DNA size marker; probes and enzyme mixed with L2: SplintR ligase + T7 RNA polymerase + miR-21; L3: L2 without T7 RNA polymerase; L4: L2 without miR-21; L5: L2 without SplintR ligase). (F) Fluorescence intensity of TO-3 mixed with the amplified product from Fig. 3E; inset figure: the fluorescence intensity of each sample captured by a camera. (G) Fluorescence intensity of TO3/Peach aptamer complex according to the OPIEA reaction time with various concentrations of miR-21. (H) Schematic illustration of the dual detection of miR-21 and U6 by OPIEA. (I) Fluorescence intensity of TO-3 with miR-21-specific probes at 650 nm (orange); DFBHI-1 T with miR-U6-specific probes at 505 nm (green) with various types of 1 nM miRs (miR-21, miR-U6, miR-25b, and miR-146a) showing the specificity of the fluorescence signal for target miRs. ***$p < 0.001$, Student's unpaired *t*-test. (For interpretation of the references to color in this figure legend, the reader is referred to the web version of this article.)

verified by monitoring RNA aptamer synthesis using T7 RNA polymerase with Pr/CD63Ab/AuNP (Fig. 3D). In this design, the template (synthesized by miR-21) encodes a peach aptamer, which binds to the TO-3 dye and produces a red fluorescence signal. Agarose gel analysis (Fig. 3E) revealed aptamer and template-aptamer complex bands only in reactions containing all essential components (miR-21, SplintR ligase, and T7 RNA polymerase; Lane 2). In contrast, omitting any single component (Lanes 3–5) abolished transcription. Interestingly, the intensity of the elongated template band in Lane 2 (complete reaction with miR-21, SplintR ligase, and T7 RNA polymerase) was notably greater than that in Lane 3 (reaction without T7 RNA polymerase), despite identical ligation conditions. This observation suggests that the presence of T7 RNA polymerase not only enables RNA aptamer synthesis but also induces a positive feedback loop within the reaction. Specifically, the transcribed RNA aptamer contains the miR-21 sequence, which can hybridize with additional donor and acceptor probes, acting as a secondary splint to facilitate further ligation events. This recursive amplification mechanism results in the accumulation of elongated templates beyond the initial ligation step, thereby enhancing the efficiency and sensitivity of the system. Importantly, this feedback amplification remains strictly target-dependent, as ligation requires precise sequence complementarity at the junction site, and formation of a functional T7 promoter occurs only upon correct target-mediated ligation. As a result, nonspecific ligation or cross-priming is effectively suppressed in the absence of the correct Exo-miR sequence.

To investigate whether this target-specific amplification process led to effective positive signal generation, the transcribed products were incubated with TO-3 dye and analyzed for fluorescence output (Fig. 3F). Consistent with the gel results, only the complete reaction (Lane 2) produced a marked increase in TO-3 fluorescence intensity (λ_{em} = 650 nm), which was also visually confirmed by the distinct red color observed under UV illumination. In contrast, reactions lacking any one of the essential components failed to generate fluorescence signals above background levels. Quantitative analysis revealed a more than 4-fold increase in fluorescence in the complete OPIEA system, demonstrating successful amplification and direct translation of the transcriptional output into measurable fluorescence signals.

To determine the optimal reaction time, the fluorescence intensity was measured at regular intervals for samples containing varying concentrations of miR-21 (0, 10 pM, 100 pM, and 1 nM) (Fig. 3G). The fluorescence signal increased over time for all concentrations, with a plateau at ~90 min. Importantly, minimal background fluorescence was observed in the 0 pM control, although a slight increase at later points suggested possible nonspecific interactions. On the basis of these results, 90 min was selected as the optimal incubation time for subsequent assays. To enable multiplex detection, we extended the OPIEA system by designing a second probe pair for miR-U6, which encodes a broccoli aptamer that binds DFHBI-1 T dye and emits green fluorescence. The orthogonality and specificity of both detection channels were tested by exposing the system to various miRs (miR-21, miR-U6, miR-25b, and miR-146a; concentration = 1 nM) (Fig. 3H–I). These results confirmed that red fluorescence light-up was selectively triggered by miR-21, while green fluorescence light-up was specific to miR-U6. No cross-reactivity or signal crosstalk was observed with off-target miRs, demonstrating excellent sequence specificity and channel separation.

To optimize Pr/CD63Ab/AuNPs for integration into the OPIEA process within ST-Exo-TAS, we investigated how DNA–AuNP conjugation affects transcription efficiency. Direct attachment of the promoter to AuNPs can obstruct access by T7 RNA polymerase, thereby significantly reducing transcriptional activity (Fig. S4A). To mitigate this steric hindrance, poly(A) spacers of varying lengths (0, 5, 10, 15, and 30 nucleotides) were inserted between the AuNP surface and the promoter sequence. As the length of the Poly A spacer increased, the overall particle size also increased, indicating that the spatial distance between the AuNPs and the promoter was effectively extended (Fig. S4B). The transcription efficiency was assessed by measuring the fluorescence signal from TO-3 dye activated by the transcribed aptamer (90 min of transcription, 10 min of incubation). When no spacer was used, the transcription efficiency decreased to approximately 20% of that of the free promoter (Fig. S4C). However, the inclusion of poly A spacers ≥15 nucleotides restored transcription levels, demonstrating that sufficient spacing enables effective polymerase binding and activity. Collectively, these findings support the rational design of the OPIEA system, confirming that miR-specific binding and isothermal transcription of fluorogenic RNA aptamers can be successfully achieved in a one-pot, single-tube format.

2.4. Dual detection of Exo-miR-21 and U6 using ST-Exo-TAS

To investigate the performance of ST-Exo-TAS for the dual detection of Exo-miR-21 and U6, various concentrations of miR-21 and U6 were applied. To test the system, various concentrations of 50 μL of miR were mixed with OPIEA solution and subjected to isothermal amplification. When successful transcription occurs, the amplified aptamer binds with its cognate fluorogenic dye and emits distinguishable fluorescence. First, we tested the signal TO-3 fluorescence intensity according to the concentration of miR-21. When miR-21 was present in the sample solution, the peach aptamer was synthesized by OPIEA. The synthesized peach aptamer could bind TO-3 fluorogenic dye and enhance the signal of the dye. As shown in Fig. 4B, the red fluorescence color of TO-3 increased as the miR-21 concentration increased. To analyze the fluorescence intensity of the TO-3/Peach aptamer, the red fluorescence was analyzed by fluorescence spectroscopy. The TO-3/Peach aptamer was excited at 637 nm and emitted red fluorescence at 650 nm. On the basis of the excitation and emission wavelengths, fluorescence spectra were recorded at various concentrations of miR-21. As the concentration of miR-21 in the sample increased, the fluorescence intensity increased, as shown in Fig. 4B. By analyzing the intensity of the maximum peak at 650 nm, a calibration curve of the red fluorescence intensity according to the miR-21 concentration was constructed and is displayed in Fig. 4C. The insert graph has a correlation coefficient (R^2) of 0.9458, corresponding to the linear relationship between the red fluorescence intensity of peach aptamer/TO-3 and the log value of the miR concentration (pM) with the equation $y = 574.3\ x + 2755$. The limit of detection (LOD) value was estimated to be 1.179 fM based on 3 σ/s (where σ is the standard deviation of the blank sample, and s is the slope of linear correction), and the limit of quantification (LOQ) was estimated to be 3.536 fM on the basis of 3 × LOD.

Similarly, the DFHBI-1 T/Broccoli aptamer fluorescence signal was analyzed to investigate the ability of OPIEA to amplify miR-U6. As shown in Fig. 4D, the green fluorescence color of DFHBI-1 T increased as the miR-U6 concentration increased. On the basis of the excitation and emission wavelengths of the DFHBI-1 T/Broccoli aptamer (Ex: 468 nm, Em: 505 nm), fluorescence spectra were recorded at various concentrations of miR-U6. As shown in Fig. 4E, the fluorescence intensity increased according to the concentration of miR-U6 in the sample. The intensity of the maximum peak at 505 nm was analyzed, and the calibration curve of the green fluorescence intensity according to the miR-U6 concentration is illustrated in Fig. 4F. The insertion graph has a correlation coefficient (R^2) of 0.9599, which corresponds to the linear relationship between the green fluorescence intensity of the DFHBI-1 T/Broccoli aptamer and the logarithmic value (pM) of the miR-U6 concentration with the equation $y = 1017\ x + 4048$. The LOD was estimated to be 843.9 aM, and the LOQ was estimated to be 2.532 fM. These results confirmed that our system could detect miR-21 and U6 by different colors of fluorescence with high sensitivity and high linearity.

We further expanded the ability of ST-Exo-TAS to enable the simultaneous detection of two target miRs in a single-tube reaction step. The detection of multiple biomarkers is frequently needed to make better decisions by reducing false-positive and false-negative results. On the basis of the high specificity of OPIEA and the availability of RNA light-up aptamers with distinct excitation and emission wavelengths, we

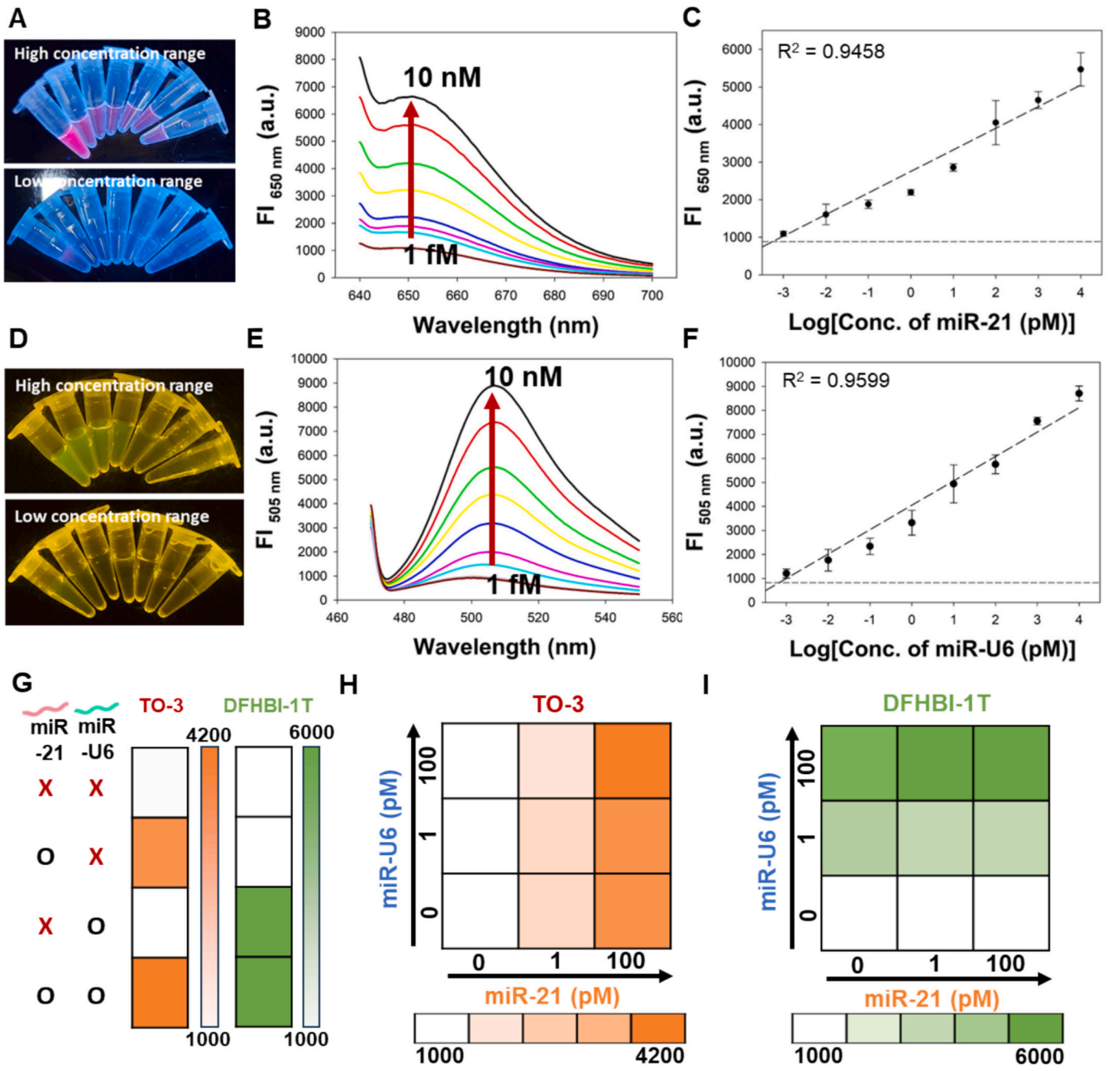


Fig. 4. Fluorescence signal analysis of miRs using ST-Exo-TAS (A) Fluorescence color of the TO-3/Peach aptamer complex at various concentrations of target miR-21 (high concentration range: from left 1 μM, 100 nM, 10 nM, 1 nM, 100 pM, 10 pM, 1 pM; low concentration range: from left 100 fM, 10 fM, 1 fM, 100 aM, 10 aM, 1 aM, 0 aM). (B) Fluorescence spectra of the fluorescence intensity of the TO-3/Peach aptamer complex at various concentrations of miR-21 ranging from 1 fM to 10 nM. (C) Calibration curve of the fluorescence intensity of various concentrations of miR-21 ranging from 1 fM to 10 nM at 650 nm. (D) Fluorescence color of the DFHBI-1 T/Broccoli aptamer complex at various concentrations of miR-U6 (high concentration range: from left 1 μM, 100 nM, 10 nM, 1 nM, 100 pM, 10 pM, 1 pM; low concentration range: from left 100 fM, 10 fM, 1 fM, 100 aM, 10 aM, 1 aM, 0 aM). (E) Fluorescence spectra of fluorescence intensity of DFHBI-1 T/Broccoli aptamer complex at various concentrations of miR-21 ranging from 1 fM to 10 nM. (F) Calibration curve of the fluorescence intensity of various concentrations of miR-U6 ranging from 1 fM to 10 nM at 505 nm. (G) Validation of the orthogonal dual detection of aptamers synthesized from ST-Exo-TAS. The presence of each probe (100 pM) was determined by the intensities of nonoverlapping fluorescence. (H) Fluorescence intensity of TO-3 observed from ST-Exo-TAS during simultaneous quantification of miR-21 and miR-U6. The assay was performed by independently spiking each target RNA into the reaction mixture at concentrations of 100 pM, 1 pM, or 0 pM. (I) Fluorescence intensity of DFHBI-1 T under the same conditions, reflecting the corresponding signal for miR-U6. All measurements were conducted in independent biological replicates ($n = 3$). Data represent the means ± SDs for independent experiments.

hypothesized that we could perform dual-detection of miRs in a single tube (Fig. S5). In our system, when miR-21 was present in the sample solution, peach aptamers were synthesized by OPIEA. Additionally, when miR-U6 was present in the sample solution, broccoli aptamers were synthesized. The synthesized aptamers (peach and broccoli) could bind to specific fluorogenic dyes (TO-3 and DFHBI-1 T) and appear in different colors (red and green, respectively). If there was no fluorescence intensity interference between the peach-TO-3 complex and broccoli-DFHBI-1 T complex, miR-21 and miR-U6 could be detected simultaneously. First, we investigated the fluorescence intensity of TO-3

(red) and DFHBI-1 T (green) in the presence and absence of target miRs (1 nM) in ST-Exo-TAS. As shown in Fig. 4G, DFHBI-1 T showed a fluorescence signal only when miR-U6 was present in the sample, and TO-3 showed a fluorescence signal independently when only miR-21 was present. These results confirmed that there was no aptamer-fluorogenic dye-specific fluorescence interference between the broccoli aptamer synthesized from miR-U6 and the peach aptamer synthesized from miR-21. As these tests employed equal concentrations of miR-21 and miR-U6 (1 nM), we next evaluated whether the system maintained performance under varying combinations of miR-21 and miR-U6 concentrations. These tests are essential for assessing the possibility of signal noise from interference when miRs are detected simultaneously in a single tube. At various concentrations of the two target RNAs (each probe was mixed into the solution independently at concentrations of 100 pM, 1 pM, and zero), the orthogonal detection system specifically reacted only to the respective target RNA and produced fluorescence free of signal impairment when mixed with various concentrations of nontarget RNA, enabling orthogonal simultaneous detection of the two miRs with different colors of fluorescence (Fig. 4H, I). These results revealed that miR-21 and miR-U6 could simultaneously be detected with good orthogonal performance in a single tube. Table 1. summarizes recent fluorescence-based biosensing devices for Exo-miR detection. In comparison to previously reported systems, ST-Exo-TAS provides a fully integrated total analysis platform that enables exosome isolation, isothermal amplification, and simultaneous dual-target detection (Exo-miR-21 and miR-U6) within a single tube, offering both superior sensitivity and significantly reduced assay time.

2.5. Performance of the ST-Exo-TAS in preclinical samples

To evaluate the diagnostic utility and analytical performance of the ST-Exo-TAS platform in biologically relevant samples, we detected and quantified two target Exo-miRs: Exo-miR-21, a well-known oncogenic marker, and Exo-miR-U6, a commonly used normalization control. Exosomes were isolated from three human breast cell lines representing distinct phenotypes: MCF-10 A (nontumorigenic epithelial), MCF-7, and SK-BR-3 (breast cancer). The morphological characteristics of each cell line are shown in Fig. S6. Prior to Exo-miR quantification, the exosomes derived from each cell type isolated by the traditional method were characterized using TEM and NTA (Fig. S7, and Fig. S8). Both TEM and NTA confirmed the presence of exosomes in the collected cell culture media, which exhibited a typical morphology and average particle sizes ranging from 197.3 to 217.8 nm.

The experimental workflow of the ST-Exo-TAS analysis in preclinical samples is illustrated in Fig. 5A, which compares the performance of the ST-Exo-TAS system against that of conventional RT–qPCR. To minimize bias due to variability in exosome secretion among the cell lines, the exosome concentrations were first measured using fluorescence-based NTA (FL-NTA). This allowed for normalization of Exo-miRs levels per a fixed number of exosomes, enabling accurate comparison of Exo-miR expression profiles independent of the cell proliferation rate or exosome release efficiency. As shown in Fig. 5B–D, both the ST-Exo-TAS and RT–qPCR results confirmed that compared with Exo-U6, Exo-miR-21 was expressed at significantly higher levels in the MCF-7- and SK-BR-3–derived exosomes, whereas this difference was not observed in the MCF-10 A-derived exosomes. These expression patterns are consistent with the established oncogenic profile of Exo-miR-21 in breast cancer and affirm that ST-Exo-TAS accurately reflects biologically relevant Exo-miR signatures. Importantly, the relative expression trends observed using ST-Exo-TAS were highly concordant with those determined by RT–qPCR, demonstrating the reliability of the platform. Despite differences in methodological complexity, both systems successfully distinguished between cancerous and noncancerous exosome sources on the basis of miRNA profiles.

Notably, ST-Exo-TAS produced slightly higher absolute signal intensities than RT–qPCR did. This difference is likely attributable to the single-tube design of ST-Exo-TAS, which eliminates RNA extraction, purification, and reverse transcription steps, all of which are potential sources of RNA loss and degradation in conventional workflows. Instead, direct amplification from intact exosomes within a closed

Table 1
Summary of recent fluorescence-based biosensing devices for Exo-miR detection.

Performed steps in the analysis device for Exo-miR detection			Detection method	Target Exo-miRs	Linear range	LOD	Total analysis time	Ref
Isolation	Amplification	Detection						
X	X	O	3D DNA Walker-Induced CRISPR/Cas12a	miR-214	50 fM to 10 nM	20.42 fM	340 min	[48]
X	X	O	DNA- hosted silver nanoclusters (DNA-AgNCs	miR-21	0.03 to 1.2 μM	15 nM	110 min	[49]
X	X	O	CRISPR/Cas13a-based probe	miR-21	0 to 30 nM	10.4 pM	240 min	[50]
X	O	O	CRISPR/Cas12a-based trans-cleavage signal amplification mechanism	Let-7a	0 to 100 pM	0.75 pM	239 min	[51]
X	O	O	The fluorescence biosensor coupled with CRISPR/Cas12a, SDR, TdT and MNPs	miR-21	500 fM to 500 pM	161 fM	175 min	[19]
X	O	O	miRNA-padlock initiated RCA and CRISPR/Cas12a	miR-21	10 fM to 1 nM	34.7 fM	440 min	[20]
X	O	O	A one-pot isothermal Cas12-based assay	miR-21	5.47 to 500 fM	1.64 fM	280 min	[21]
X	O	O	A nanoplatform-based ratiometric fluorescent sensor	miR-92a-3p	0.1 to 50 pM	0.047 pM	280 min	[22]
X	O	O	Au NCs/UiO-66-NH_2	piR-823	0.04 to 4 pM	10.2 fM	450 min	[23]
X*	O	O	Fluorescent biosensor based on DSN and Nt.*Bbv*CI mediated dual-signal amplification reaction	miR-21	0.5 to 100 fM	0.34 fM	320 min	[24]
X	O	O	Nucleic acid amplification circuit-based hydrogel (NACH)	miR-21 miR-99a (Dual)	1 fM to 100 pM 1 fM to 100 pM	1 fM 1 fM	240 min	[25]
O	**O**	**O**	**ST-Exo-TAS (This study)**	**miR-21 miR-U6 (Dual)**	**1 fM to 10 nM 1 fM to 10 nM**	**1.179 fM 843.9 aM**	**150 min**	**This study**

* Total analysis time = The time required from exosome isolation in samples to the final analysis step. * X* = Exosomes were isolated using conventional methods, but an additional Exo-miR extraction step was performed in device.

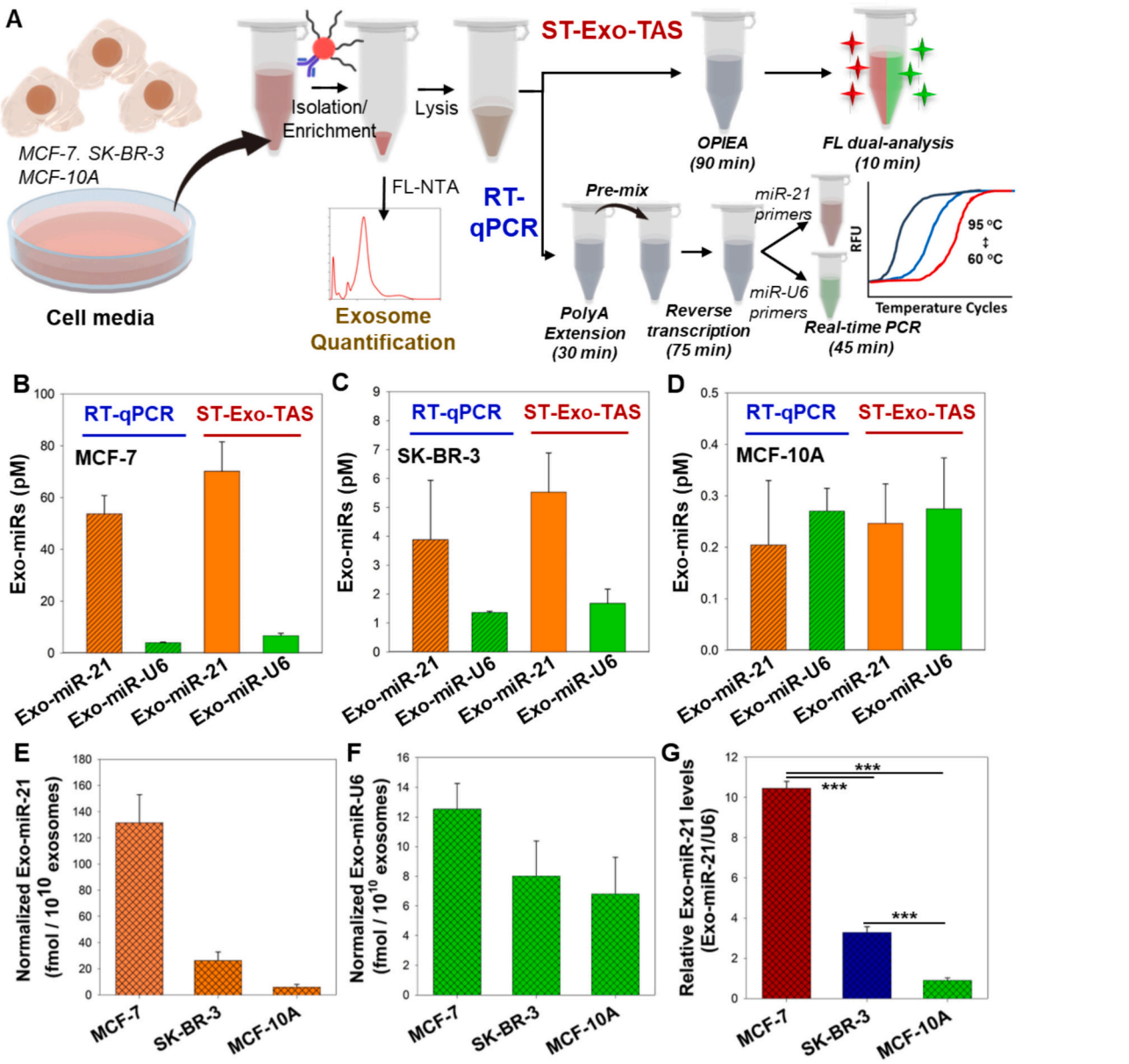


Fig. 5. (a) Schematic illustration of isolated exosome counting and comparative analysis of Exo-miR-21 and U6 in exosomes isolated from cell culture medium by ST-Exo-TAS and RT–qPCR. Quantitative Exo-miR analysis results of ST-Exo-TAS and RT–qPCR from (B) MCF-7, (C) SK-BR-3, and (D) MCF-10 A-derived exosomes. Normalization strategies for detecting (E) Exo-miR-21 and (F) Exo-miR-U6 from the results of ST-Exo-TAS according to the number of exosomes. (G) Relative expression levels of Exo-miR-21 and Exo-miR-U6 in exosomes derived from MCF-7, SK-BR-3, and MCF-10 A cells. All measurements were conducted in independent biological replicates ($n = 3$). Data represent the means ± SDs for independent experiments. ***$p < 0.001$, Student's unpaired t-test.

system minimizes sample handling, preserves RNA integrity, and enhances detection sensitivity. It is also important to consider the exosome input quantities used for each cell line, which were measured by fluorescence nanoparticle tracking analysis (FL-NTA) prior to analysis. Specifically, 5.3×10^9 particles/mL exosomes were isolated from MCF-7 cells, 2.1×10^9 particles/mL exosomes were isolated from SK-BR-3 cells, and only 0.4×10^9 particles/mL exosomes were isolated from MCF-10 A cells. Despite this variation in exosome abundance, both ST-Exo-TAS and RT–qPCR generated comparable diagnostic results after normalization, further demonstrating that ST-Exo-TAS provides robust and consistent Exo-miR quantification even with variable exosome input levels.

To more rigorously evaluate diagnostic performance, we normalized the raw Exo-miRs signal intensities by exosome count and calculated Exo-miR levels in fmol per 10^{10} exosomes. As shown in Fig. 5E, the normalized Exo-miR-21 levels were the highest in exosomes from MCF-7 cells (131.6 ± 21.3 fmol), followed by those from SK-BR-3 cells (26.4 ± 6.5 fmol), and lowest in those from MCF-10 A cells (6.1 ± 1.9 fmol). These values reflect a 21.5-fold dynamic range between cancerous and noncancerous exosome sources, underscoring the suitability of Exo-miR-21 as a cancer biomarker. In contrast, the normalized Exo-miR-U6 levels showed minimal variation across cell types (Fig. 5F), with differences <1.84-fold, reinforcing its validity as a robust internal reference Exo-miR for normalization (Exo-miR-U6 in 10^{10} exosomes derived from MCF-7 = 12.5 ± 1.7 fmol, SK-BR-3 = 8.0 ± 2.4 fmol, and MCF-10 A = 6.8 ± 2.5 fmol). To validate the suitability of Exo-miR-U6 as an internal reference, we further examined the relationship between exosome abundance and Exo-miR-U6 levels across different cell-derived exosome sources. As a result, the Exo-miR-U6 signal exhibited a strong linear correlation with exosome number over the tested range, regardless of

the cellular origin of the exosomes (Fig. S9). Importantly, the slope of this correlation was comparable among MCF-7, SK-BR-3, and MCF-10 A–derived exosomes, indicating that Exo-miR-U6 abundance scales proportionally with exosome count rather than reflecting cell type–specific regulation. These results support the use of Exo-miR-U6 as a robust internal reference for normalizing Exo-miR signals and compensating for variations in exosome numbers.

Based on these results, we implemented a ratiometric normalization strategy using the Exo-miR-21/Exo-miR-U6 expression ratio to eliminate potential bias introduced by differences in exosome loading. This ratio allows for within-sample control without the need for separate calibration standards. As illustrated in Fig. 5G, the normalized expression ratio differed markedly among the three cell types: the percentage of MCF-7 exosomes was 10.5 ± 0.3, followed by that of SK-BR-3 (3.30 ± 0.3), while the baseline ratio of MCF-10 A exosomes was 0.91 ± 0.11. These results confirm that ST-Exo-TAS can distinguish between exosomes originating from cancerous cells and those originating from noncancerous cells on the basis of their normalized Exo-miR signature,

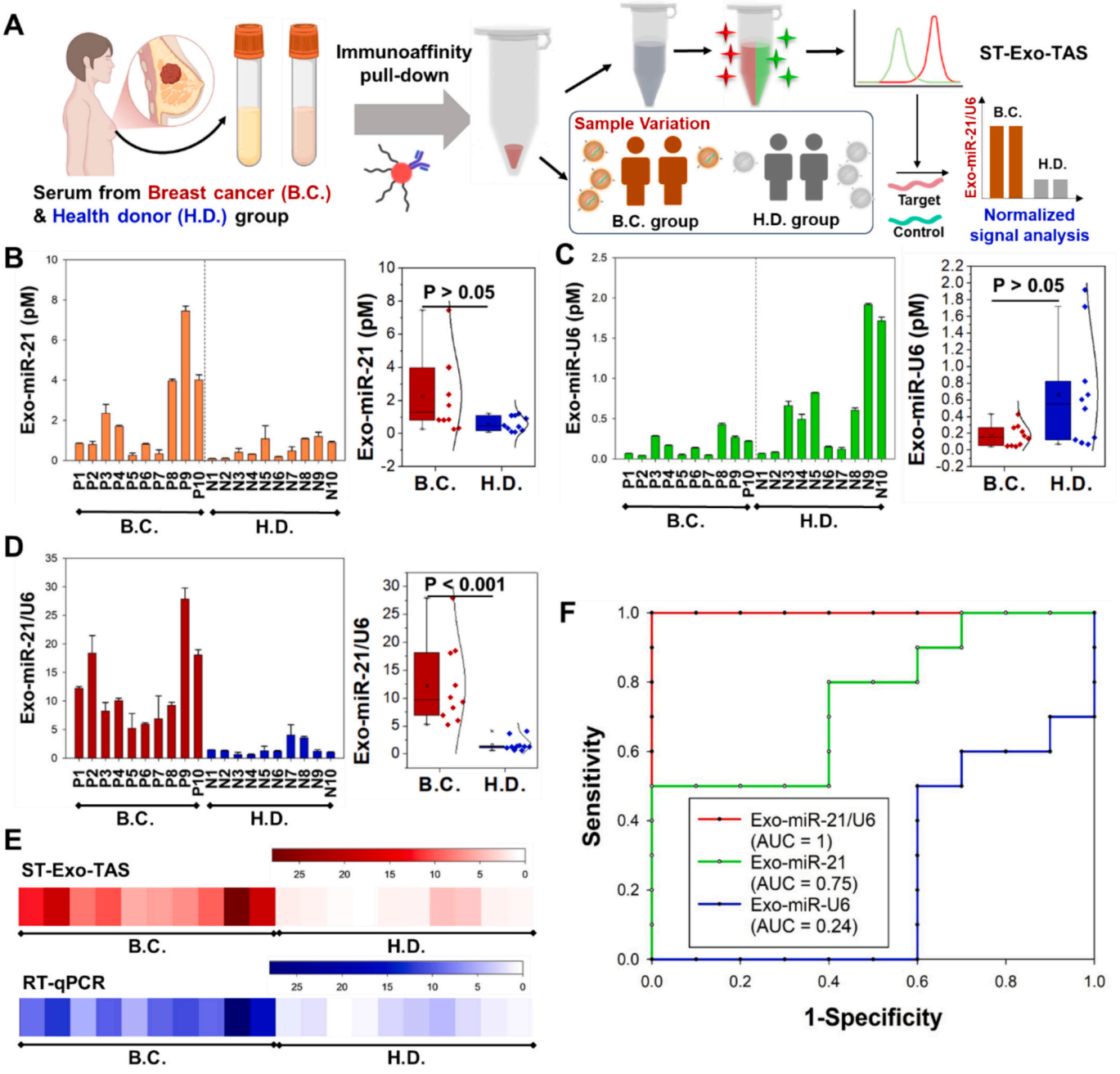


Fig. 6. (A) Schematic illustration of the ST-Exo-TAS strategy for detecting target Exo-miRs in plasma samples from breast cancer patients (B.C.: P1–P10, n = 10) and healthy donors (H.D.: N1–N10, n = 10). The platform employs miR-U6–based normalization of Exo-miR-21 to compensate for sample-to-sample variation in exosome content. (B) Analyzed concentration of Exo-miR-21 in plasma samples by ST-Exo-TAS and (C) Exo-miR-U6. (D) Comparison of the relative expression levels of Exo-miR-21 and Exo-miR-U6 in exosomes derived from the B.C. group and H.D. group according to the results of ST-Exo-TAS. Data represent the means ± SDs for independent experiments. (E) Heatmap of the expression of Exo-miR-21 relative to that of Exo-miR-U6 in plasma samples determined using ST-Exo-TAS (red) and RT–qPCR (blue). (F) ROC analysis for the performance of the cancer diagnosis using the value of Exo-miR-21/U6. Exo-miR-21 and Exo-miR-U6 were analyzed by ST-Exo-TAS. All measurements were conducted in independent biological replicates (n = 3). AUC values with 95% confidence intervals were calculated using nonparametric bootstrap resampling. (For interpretation of the references to color in this figure legend, the reader is referred to the web version of this article.)

which is independent of exosome concentration. Furthermore, to evaluate the practical robustness of the ST-Exo-TAS platform, we assessed intra- and inter-assay precision, batch-to-batch consistency of independently prepared Pr/CD63Ab/AuNPs, and storage stability using cell-derived exosomes (Table S3, Fig. S10, Fig. S11). The results showed good reproducibility and stability over time (>80%), with minimal variation observed across repeated measurements and storage periods.

Overall, this preclinical validation demonstrates that compared with conventional RT–qPCR, ST-Exo–TAS offers several key advantages: (1) higher analytical sensitivity due to single-tube processing, (2) improved RNA preservation, (3) dual-target detection with built-in normalization, and (4) a fast and simple workflow with minimum instruments. These features position ST-Exo-TAS as a powerful and practical diagnostic platform for accurate Exo-miR profiling, particularly in the context of liquid biopsy-based early cancer detection.

2.6. Performance of the ST-Exo-TAS in clinical samples

To demonstrate the potential of ST-Exo-TAS for clinical application, our group ultimately applied ST-Exo-TAS for the dual detection of Exo-miR-21 and Exo-miR-U6 in clinical samples from plasma samples (plasma samples from breast cancer patients (B.C.) ($n = 10$) and healthy donors (H.D.) (n = 10)) collected from the Biobank of Jeonbuk National University Hospital and compared the RT–qPCR results (Fig. 6A). This study was approved by the institutional review board of Jeonbuk National University Hospital (IRB number, CUH2024–10–039-003) and was performed in compliance with the Declaration of Helsinki. Written informed consent was obtained from the Biobank of Jeonbuk National University Hospital.

Before clinical application, we evaluated the exosome isolation performance of the immunoaffinity-based Pr/CD63Ab/AuNPs system in complex biological matrices. To assess selectivity and resistance to biological interference, the isolation efficiency of our system was quantitatively compared with that of a commercially available non-immunoaffinity-based exosome isolation kit using both cell culture media and human plasma samples. When exosomes were isolated from cell culture media, the Pr/CD63Ab/AuNPs system achieved approximately 83% isolation efficiency relative to the commercial kit (Invitrogen) (Fig. S12). In contrast, exosome isolation from human plasma resulted in a slightly reduced efficiency of approximately 75%. This reduction is attributed to the presence of abundant co-existing biological components in plasma, such as lipoproteins and plasma proteins, which can interfere with antibody–exosome interactions and partially limit immunoaffinity capture efficiency. Despite these complex biological interferences, the observed difference in isolation efficiency between cell culture media and plasma samples was not substantial, indicating that the Pr/CD63Ab/AuNPs system remains effective for isolating plasma-derived exosomes.

ST-Exo-TAS was applied to clinical samples, and Exo-miR-21 and Exo-miR-U6 were detected and analyzed. As shown in Fig. 6B, Exo-miR-21 levels were generally higher in the B.C. group than in the H.D. group. However, complete separation between the two groups was not achieved, and several overlapping data points were observed. Statistical analysis using a two-tailed *t*-test yielded a *p*-value of 0.051, indicating a borderline statistical difference in Exo-miR-21 expression between the two groups. To further investigate the source of this variability, Exo-miR-U6 levels were analyzed (Fig. 6C). In some H.D. samples, Exo-miR-U6 levels were higher than those observed in the B.C. group. Statistical analysis yielded a p-value of 0.052, again indicating a borderline statistical difference rather than a disease-specific change. This elevation in Exo-miR-U6 levels is likely attributable to variations in the absolute number of exosomes present in individual plasma samples. Differences in sample collection conditions, plasma quality, and donor physiology may contribute to heterogeneity in exosome yield, thereby affecting the apparent levels of both target and reference Exo-miRs. Although direct NTA-based quantification of exosome concentration in the clinical samples was not feasible due to IRB-mandated sample disposal, independent analyses demonstrated a strong correlation between exosome abundance and Exo-miR-U6 signal. These results support the interpretation that variations in Exo-miR-U6 levels primarily reflect differences in exosome yield rather than disease-associated effects.

Accordingly, samples with low exosome abundance in the B.C. group may exhibit lower apparent Exo-miR-21 signals than samples from the H.D. group with higher exosome counts. This observation highlights the importance of appropriate normalization for Exo-miR-21 quantification and provides a clear rationale for the ratiometric Exo-miR-21 and Exo-miR-U6 strategy employed in the ST-Exo-TAS platform.

On the basis of these assumptions and results, we normalized Exo-miR-21 to Exo-miR-U6 using the results from ST-Exo-TAS. As shown in Fig. 6D, compared with that in the H.D. group, the normalized signal in the B.C. group was much greater. Using Student's *t*-test, we detected a significant difference in the average Exo-miR-21/U6 ($p < 0.001$) signal level between the B.C. group and the H.D. group. These results emphasize the need for standardized biomarker analysis through dual detection. We further validated the clinical applicability and reliability of the ST-Exo-TAS platform by comparing its performance with that of conventional RT–qPCR analysis. A heatmap was generated to visualize the relative expression levels of Exo-miR-21 normalized to those of Exo-miR-U6, as measured by both methods (Fig. 6E). The expression patterns observed using ST-Exo-TAS closely matched those obtained from RT–qPCR, indicating a high degree of consistency between the two approaches. These results demonstrate that ST-Exo-TAS can be used to reliably quantify Exo-miRs expression and is suitable for clinical sample analysis. Furthermore, a receiver operating characteristic (ROC) curve for determining the diagnostic accuracy of these assays for detecting Exo-miR-21 and Exo-miR-U6 was constructed (Fig. 6F). The area under the curve (AUC) was 0.75 (95% CI: 0.50–0.94) for Exo-miR-21 and 0.24 (95% CI: 0.05–0.51) for Exo-miR-U6. However, the AUC value was 1.00 (95% CI: 1.00–1.00) for the signal normalized by Exo-miR-21/U6. The corresponding AUC values are reported with 95% confidence intervals to account for uncertainty arising from the limited cohort size. This finding indicates that dual detection and standardization using ST-Exo-TAS substantially improved diagnostic discrimination between breast cancer patients and healthy donors.

In addition to the clear separation between breast cancer patients and healthy donors, a limited but consistent trend was observed within the breast cancer cohort. Specifically, patients with more advanced local disease, including T2 tumors and nodal involvement, tended to exhibit higher Exo-miR-21/U6 ratios compared with early-stage cases (Fig. S13). Although the small cohort size precludes formal statistical stratification, this tendency aligns well with numerous previous studies reporting progressive increases in Exo-miR-21 expression, normalized to Exo-miR-U6, with tumor advancement and aggressive clinicopathologic features [37,52–56]. Therefore, the trend observed in the present dataset is broadly consistent with established literature, supporting the biological relevance of the Exo-miR-21/U6 ratio as a progression-associated exosomal biomarker.

Although the present clinical cohort consisted of only ten breast cancer patients and ten healthy donors, this sample size was determined by the scope of the IRB-approved plasma collection and was intended for an exploratory feasibility assessment rather than definitive clinical validation. The limited cohort size constrains statistical power and precludes extensive subgroup analyses, which may affect the robustness of individual biomarker-based conclusions. Nevertheless, by employing ratiometric normalization of Exo-miR-21 to Exo-miR-U6 within a single reaction tube, ST-Exo-TAS effectively mitigated inter-sample variability arising from differences in exosome abundance and RNA loading. This normalization strategy enabled clear diagnostic separation between cancer and noncancer groups even within a limited dataset, supporting the clinical relevance of the platform at the feasibility stage. The effect-size and variance estimates obtained from this pilot cohort will inform

power calculations and study design for future large-scale clinical validation, and larger, well-characterized patient cohorts will be required to fully establish diagnostic robustness and generalizability.

3. Conclusion

In this study, we developed a fully integrated single-tube Exo-miR total analysis system (ST-Exo-TAS) that enables streamlined, dual-target detection of Exo-miRs (Exo-miR-21 and miR-U6) with high sensitivity, specificity, and operational simplicity. By integrating immunoaffinity-based exosome capture with OPIEA via Pr/CD63Ab/AuNPs, ST-Exo-TAS performs exosome isolation, Exo-miR ligation, transcription, and dual-color fluorescence detection within a single reaction tube, eliminating the need for stepwise sample transfer or thermal cycling. The system achieved attomolar-level sensitivity (LOD = 1.179 fM for miR-21 and 843.9 aM for miR-U6), with strong sequence specificity and minimal cross-reactivity. Comparative validation with conventional RT–qPCR further confirmed the analytical accuracy of ST-Exo-TAS across both preclinical and clinical samples. In addition, the entire assay can be completed in under 2.5 h using only basic laboratory equipment, highlighting its suitability for decentralized and point-of-care applications. Normalization of Exo-miR-21 to Exo-miR-U6 within the same tube enhanced diagnostic resolution, enabling robust discrimination between breast cancer-derived and noncancerous exosomes regardless of exosome abundance. While the current platform is limited to two targets due to aptamer–dye spectral constraints, future development of orthogonal light-up aptamers with non-overlapping emission profiles will facilitate multiplexed detection of three or more Exo-miRs in a single reaction. Such expansion will enable broader molecular profiling and further improve diagnostic accuracy. Beyond analytical performance, several considerations are important for practical deployment. The closed-tube configuration, minimal manual handling, and lack of thermal cycling align with key requirements for point-of-care testing. For successful commercialization, batch-consistent fabrication of Pr/CD63Ab/AuNP nanoprobes, long-term storage stability, and standardized reaction cartridges will be essential to ensure reproducibility and regulatory compliance. Also, future integration of ST-Exo-TAS into automated analytical devices could further enhance operational robustness by minimizing manual handling steps and reducing user-induced variability. Taken together, these findings indicate that ST-Exo-TAS offers a rapid, contamination-free, and instrument-light solution for sensitive Exo-miR detection. With continued optimization of multiplexing and manufacturing, the ST-Exo-TAS framework holds strong potential as a practical tool for point-of-care diagnostics, liquid biopsy, and noninvasive monitoring of cancer and other diseases.

4. Experimental section

4.1. Materials

MCF-7 and SK-Br-3 cells were obtained from the Korea Cell Link Bank (Korea), and MCF-10 A cells were obtained from American Type Culture Collection (ATCC, USA). RPMI 1640 medium (LM 011–03) and phosphate-buffered saline (PBS) were purchased from Welgene (Korea). DMEM/F12 medium (11330032) and exosome-depleted fetal bovine serum (A2720801) were purchased from Gibco Co. (USA). Recombinant human insulin (I9278), recombinant human epidermal growth factor (EGF) (E9644), hydrocortisone (H6909), and cholera toxin (C8052) were purchased from Sigma–Aldrich (USA). Total exosome isolation kits were purchased from QIAGEN (Germany), Cell Guidance Systems (USA), System Bioscience (CA), and Invitrogen (USA). AuNP (30 nm) was purchased from BBI International (UK). Triethylene glycol mono-11-mercaptoundecyl ether (TEG), potassium chloride (KCl), (5Z)-5-[(3,5-difluoro-4-hydroxyphenyl) methylene]-3,5-dihydro-2-methyl-3-(2,2,2-trifluoroethyl)-4H-imidazol-4-one (DFHBI-1 T), and polyoxyethylene sorbitol ester (Tween 20) were purchased from Sigma Aldrich (USA). TO3-3PEG-Biotin fluorogenic dye was purchased from Applied Biological Materials, Inc. (CA). Bovine serum albumin (BSA) was purchased from Thermo Fisher (USA). Anti-CD63 monoclonal antibody (sc-5275) was purchased from Santa Cruz Biotechnology Inc. (USA). Goat anti-mouse IgG antibody conjugated with Cyanine3 (A10521) and goat anti-mouse IgG antibody conjugated with Alexa 488 (A28175) were purchased from Invitrogen (USA). T7 RNA polymerase (M0251S), ribonucleotide triphosphate solution mix (rNTP) (N0466S), and SplintR ligase (M0375S) were purchased from New England Biolabs (NEB, USA). RiboLock RNase Inhibitor (40 U/μL) (EO0381) was purchased from Thermo Fisher (USA). Designed DNA fragments were purchased from Bionics (Korea), and miR and DEPC water were purchased from Bioneer (Korea). All the designed sequences of the DNA fragment and target miR are listed in Table S4, and the expected secondary structure of the DNA/RNA fragment simulated by NUPACK is described in Fig. S14 and Fig. S15.

4.2. Synthesis of Pr/CD63Ab/AuNPs

Pr/CD63Ab/AuNPs were synthesized by sequentially immobilizing anti-CD63 antibodies and thiolated single-stranded promoter DNA onto gold nanoparticles (AuNPs). Briefly, 1 mL of 30 nm citrate-stabilized AuNP solution was mixed with 5 μL of anti-CD63 antibody (200 μg/mL) and incubated at 25 °C for 15 min to allow for physical adsorption of the antibody (forming CD63Ab/AuNP). The optimal volume of antibody was selected by observing the color change of AuNPs containing different antibody concentrations in the presence of NaCl (Fig. S16). Afterward, 15 μL of thiol-modified promoter oligonucleotide (10 μM) was added to the CD63Ab/Au solution and incubated at 25 °C for 30 min under vigorous stirring to facilitate Au—S bond formation. To block nonspecific adsorption and stabilize the surface, 10 μL of tetraethylene glycol (TEG, 80 μM) was added to the reaction mixture and incubated for an additional 60 min at 25 °C with continuous stirring. After surface modification, the unbound promoter DNA and excess antibody were removed by centrifugation at 8000 rpm (6000 *g*) for 10 min at 25 °C. The supernatant was discarded, and the pellet was resuspended in 1 mL of distilled water. This washing step was repeated once. The resulting Pr/CD63Ab/AuNPs were stored in the dark at 4 °C until further use.

4.3. Cell culture and isolation of exosomes using Pr/CD63Ab/AuNPs

Human breast cancer cell lines (MCF-7 and SK-BR-3) and a non-tumorigenic mammary epithelial cell line (MCF-10 A) were cultured under standard conditions. MCF-7 and SK-BR-3 cells were maintained in RPMI-1640 medium supplemented with 10% fetal bovine serum (FBS) and 1% penicillin–streptomycin, while MCF-10 A cells were cultured in DMEM/F12 medium supplemented with 5% FBS, 10 ng/mL epidermal growth factor (EGF), 0.5 μg/mL hydrocortisone, 100 ng/mL cholera toxin, and 10 μg/mL insulin. All the cells were incubated at 37 °C in a humidified atmosphere with 5% CO_2. To harvest the exosomes, the cells were cultured in 100-mm dishes until they reached 70–90% confluence. The culture medium was aspirated, and the cells were gently washed three times with 10 mL of phosphate-buffered saline (PBS) to remove residual serum-derived exosomes. The medium was then replaced with serum-free RPMI or DMEM/F12 (as appropriate), and the cells were incubated for an additional 24 h. For immunoaffinity pulldown-based isolation, 1 mL of cell-free conditioned medium was transferred to a 1.5 mL microcentrifuge tube and incubated with 200 μL of Pr/CD63Ab/AuNPs for 30 min at room temperature with gentle agitation. Exosome-bound nanoprobes were isolated by centrifugation at 8000 rpm (6000 *g*) for 10 min. The supernatant was discarded, and the resulting exosome–Pr/CD63Ab/AuNP complex was resuspended in distilled water or used immediately for downstream analysis. All exosome–nanoprobe complexes were stored at 4 °C in the dark until further use.

4.4. Exosome counting

To analyze the exosomes from human cells, and not exosomes from FBS, fluorescence nanoparticle tracking analysis (FL-NTA) was performed with immunofluorescence labeling of the isolated exosomes. Exosomes isolated from MCF-7, SK-Br-3, and MCF-10 A cells were first incubated with an anti-CD9 antibody for 1 h at 25 °C and then reacted with a goat anti-mouse IgG antibody conjugated with Cyanine3. Exosome particles present in the filtrate samples were analyzed by a NanoSight NS300 system (Malvern Instruments Ltd., U.K.) configured with a 532-nm laser and a high-sensitivity CMOS camera (OrcaFlash2.8, Hamamatsu C11440, NanoSight Ltd.). Videos were collected and analyzed using NTA software (version 2.3; build 0025), with the camera level set to 14 and the detection threshold set to 3. A 565-nm longpass filter was used to measure the number of fluorescently labeled exosomes. Each sample was diluted in distilled water. By monitoring the trajectory of exosome movement, the particle number and size distribution were obtained from averaged measurements of 3 videos, each with a duration of 60 s.

4.5. Transmission electron microscopy

Exosomes were negatively stained with UranyLess EM stain (Electron Microscopy Sciences, UK) for transmission electron microscopy (TEM) analysis. All procedures were performed according to the manufacturer's protocol. Briefly, a carbon-coated 200 mesh copper grid (Ted Pella Inc., CA) was discharged for 1 min by a glow discharger, after which the exosomes were dropped onto the copper grid at 25 °C for 5 min. After that, the exosomes were stained with 10 μM uranyl acetate solution on the surface of the grid, followed by quick washing with distilled water to remove excess Uranyless EM stain. The grid was dried at 25 °C, viewed, and analyzed using a JEOL1010 microscope (Japan).

4.6. miR-mediated single-strand DNA ligation assay using SplintR ligase

The single-stranded DNA ligation assay was performed using SplintR ligase, following a modified protocol based on previous study [57]. The reaction mixture (total volume: 20 μL) contained 2 μL of DNA probe mixture (acceptor and donor, 10 μM each; final concentration: 1 μM each), 2 μL of synthetic miR-21 at varying concentrations, 2 μL of 10× SplintR ligase buffer, 1 μL of SplintR ligase (25,000 U/mL; New England Biolabs), and 13 μL of DEPC-treated water. The reaction was incubated at 37 °C for 60 min to allow for template-guided ligation between the donor and acceptor DNA probes. To terminate the reaction, the mixture was heated at 95 °C for 5 min. To visualize the ligation products, 4 g of agarose powder was dissolved in 100 mL of 0.5× TBE buffer and heated until fully melted. Approximately 25 mL of molten agarose solution was poured into a 55 × 60 × 0.5 mm^3 casting tray and allowed to solidify at room temperature. The gel was placed into an electrophoresis chamber filled with 0.5× TBE buffer, and the loading wells were positioned toward the cathode side. Next, 8 μL of each reaction sample and 2 μL of DNA ladder were loaded into individual wells. Electrophoresis was conducted under dark conditions at 100 V for 40 min. After electrophoresis, the gel was stained with 1× SYBR Gold nucleic acid stain (Invitrogen) for 60 min in the dark. Images of the stained gel were acquired using a gel documentation system to assess the presence and size of the ligated DNA products.

4.7. miR-mediated OPIEA confirmation using gel electrophoresis

OPIEA analysis was conducted by mixing 20 μL of 100 nM target miR-21 with 5 μL of Pr/CD63Ab/AuNP solution and 25 μL of OPIEA solution. The OPIEA solution was composed of 2 μL of DNA probe mixture for miR-21 (acceptor and donor, 10 μM each; final concentration: 1 μM each), 1 μL of SplinR ligase (25,000 U/mL), 5 μL of 10× SplintR ligase buffer, 2.5 μL of T7 RNA polymerase (50,000 U/mL), 10 μL of 5× T7 RNA polymerase buffer, 1 μL of RNase inhibitor (40,000 U/mL), and 2.5 μL of rNTP mix (25 mM of each rNTP), and 1 μL of DEPC water. During the experiments, specific components were not added according to the experimental conditions, and DEPC water was added. The mixture was incubated at 37 °C for 120 min. To visualize the ligation products, 4.5 g of agarose powder was dissolved in 100 mL of 0.5× TBE buffer and heated until fully melted. Approximately 25 mL of molten agarose solution was poured into a 55 × 60 × 0.5 mm^3 casting tray and allowed to solidify at room temperature. The subsequent gel electrophoresis method was the same as the previous method.

4.8. Fluorescence analysis of aptamer binding with TO-3 and DFHBI-1 T

To evaluate the fluorescence response of the transcribed RNA aptamers, we conducted a binding assay using their respective fluorogenic dyes. Fluorogenic dye solutions were first prepared in 3 M KCl: 100 μM DFHBI-1 T for the broccoli aptamer and 5.6 μM TO3-3PEG-Biotin for the peach aptamer. For each measurement, 100 μL of the RNA aptamer solution generated via OPIEA was mixed with 300 μL of the appropriate dye solution (for imaging, 50 μL of the amplified RNA aptamers were mixed with 50 μL of fluorogenic dye solution). The mixture was incubated at 25 °C for 10 min to allow for sufficient binding between the aptamer and fluorogenic dye. Following incubation, fluorescence spectra were acquired using a HITACHI F-7000 fluorescence spectrophotometer (Japan) equipped with FL Solutions software. For the peach aptamer–TO-3 complex, fluorescence was measured with an excitation wavelength of 637 nm and an emission scan range of 640–700 nm. Both the excitation and the emission slits were set to 10 nm, with a photomultiplier tube (PMT) voltage of 620 V and a scan speed of 240 nm/min. For the broccoli aptamer–DFHBI-1 T complex, the excitation was set to 468 nm, and the emission range was 470–550 nm, with identical slit widths and scan speeds except for the PMT voltage of 680 V. The resulting fluorescence intensities were analyzed to assess the specificity and sensitivity of aptamer-based signal generation corresponding to the presence of Exo-miR-21 and Exo-miR-U6.

4.9. ST-Exo-TAS assay for Exo-miR detection in samples

ST-Exo-TAS-based sensitive simultaneous quantitative miR analysis of exosomes was conducted in three steps: exosome isolation/enrichment, isothermal exosome miR amplification and dual-fluorescence miR detection. First, exosomes were isolated from cell medium by an immunoaffinity pull-down method using Pr/CD63Ab/Au. In more detail, 1 mL of cell and debris-free cell medium (by centrifugation at 2000 *g* for 30 min) was mixed with 200 μL of Pr/CD63Ab/Au and incubated for 30 min or more at 24 °C. The mixture was isolated by centrifugation at 6000 *g* for 10 min, after which the supernatant was removed. To the isolated exosome-Pr/CD63Ab/Au complex pellet, 50 μL of 1% Triton X-100 was added, and the mixture was incubated for 10 min at 37 °C for exosome lysis. Second, to conduct OPIEA analysis, 50 μL of prepared OPIEA solution, SplintR ligase, SplintR ligase buffer, RNase inhibitor, T7 RNA polymerase, T7 RNA polymerase buffer, and rNTP was mixed with exosome lysis solution. The concentration and volume of each solution are described in Table S5. The 100 μL total volume of solution was incubated at 37 °C for 90 min for OPIEA analysis. Third, after amplification, 300 μL of fluorogenic dyes for aptamer light-up (100 μM DFHBI-1 T for broccoli aptamer and 5.6 μM TO3-3PEG-Biotin for peach aptamer in 3 M KCl) was added to the amplified RNA aptamer solution and incubated for 10 min. Finally, the fluorescence intensity (green, red) of 400 μL of solution was analyzed by a fluorescence spectrometer, which was the same as that described in Section 4.8.

4.10. RT–qPCR

Before the qPCR, the cDNAs were synthesized from Exo-miRs/and the control miR was synthesized by the conventional poly A tailing

method with reverse transcription. First, 2 μL of extracted miRNA sample was mixed with 2 μL of 10 mM ATP, 2 μL of *E. coli* poly(A) polymerase reaction buffer, 1 μL of *E. coli* poly(A) polymerase (NEB), and 13 μL of DEPC water. The poly A tailing reaction was conducted at 37 °C for 30 min. Then, 10 μL of elongated miRNA was mixed with 1 μL of 10 μM universal RT primer and 9 μL of DEPC water and incubated for 5 min at 70 °C before it was placed directly on ice. First, 10 μL of the previous solution was mixed with 10 μL of 2× AccuPower RT Master Mix. cDNA synthesis was conducted by incubating the mixture for 60 min at 42 °C and 5 min at 95 °C. After the synthesis of cDNA, RT–qPCR was performed to quantify the target miRNA by following the protocol of a conventional RT–qPCR kit (Accupower® 2× Greenstar™ qPCR Master Mix) (Bioneer, KR). The reactions in this work were performed on a Bio-Rad CFX Connect (USA) PCR instrument.

4.11. Clinical sample acquisition

Human plasma samples ($n = 20$) collected from B.C. patients and H. D. were provided by the Biobank of Jeonbuk National University Hospital, and the study protocol was approved by the Ethics Committee of the Korea Research Institute of Bioscience and Biotechnology (IRB number, CUH2024–10–039-003). The study included 10 patients with a clinical diagnosis of B.C. and 10 healthy individuals. Patient samples were classified on the basis of pathological results obtained by using the TNM staging system with human epidermal growth factor receptor 2 (HER2). In accordance with the ICD-10 guidelines, B.C. patients were medically classified as C50, while healthy individuals were classified as Z00. Their pathological information was verified by immunohistochemical staining and is summarized in Table S6. Statistical analyses were performed using Student's *t*-test and ROC curve analysis, and 95% confidence intervals for AUC values were estimated using nonparametric bootstrap resampling.

CRediT authorship contribution statement

Myeong-Jun Lee: Writing – review & editing, Writing – original draft, Visualization, Validation, Resources, Methodology, Investigation, Formal analysis, Data curation. **Jeong-Hyeop Shin:** Writing – review & editing, Investigation, Formal analysis. **Seung-Hun Jung:** Writing – review & editing, Methodology, Investigation. **Ha Rim Ahn:** Writing – review & editing, Resources. **Young Jo Kim:** Writing – review & editing, Investigation. **Jeong-Woo Choi:** Writing – review & editing, Investigation. **Jin-Ha Choi:** Writing – review & editing, Writing – original draft, Supervision, Project administration, Conceptualization. **Byung-Keun Oh:** Writing – review & editing, Writing – original draft, Supervision, Project administration, Funding acquisition, Conceptualization.

Declaration of competing interest

The authors declare that they have no known competing financial interests or personal relationships that could have appeared to influence the work reported in this paper.

Acknowledgements

This research was supported by the National Research Foundation of Korea (NRF) grant funded by the Korean government (MSIT) (RS-2022-NR069336) and by the Korea government (MSIT)(No. RS-2024-00466474), and supported by the National NanoFab Center(NNFC) grant funded by the Korea government (MSIT) (No. RS-2024-00440049).

The biospecimens and data used in this study were provided by the Biobank of Jeonbuk National University Hospital, a member of the Korea Biobank Network, which is supported by the Ministry of Health, Welfare and Family Affairs. All samples derived from the Korea Biobank Network were obtained with informed consent under institutional review board-approved protocols.

Appendix A. Supplementary data

Supplementary data to this article can be found online at https://doi.org/10.1016/j.cej.2026.173140.

Data availability

Data will be made available on request.

References

[1] W. Hamilton, F.M. Walter, G. Rubin, R.D. Neal, Improving early diagnosis of symptomatic cancer, Nat. Rev. Clin. Oncol. 13 (12) (2016) 740–749, https://doi.org/10.1038/nrclinonc.2016.109.

[2] D. Crosby, S. Bhatia, K.M. Brindle, L.M. Coussens, C. Dive, M. Emberton, S. Esener, R.C. Fitzgerald, S.S. Gambhir, P. Kuhn, T.R. Rebbeck, S. Balasubramanian, Early detection of cancer, Science 375 (6586) (2022) eaay9040, https://doi.org/10.1126/science.aay9040.

[3] G. Berumen Sánchez, K.E. Bunn, H.H. Pua, M. Rafat, Extracellular vesicles: mediators of intercellular communication in tissue injury and disease, Cell Commun. Signal. 19 (1) (2021) 104, https://doi.org/10.1186/s12964-021-00787-y.

[4] R. Kalluri, V.S. LeBleu, The biology, function, and biomedical applications of exosomes, Science 367 (6478) (2020) eaau6977, https://doi.org/10.1126/science.aau6977.

[5] N. Ebrahimi, F. Faghihkhorasani, S.S. Fakhr, P.R. Moghaddam, E. Yazdani, Z. Kheradmand, F. Rezaei-Tazangi, S. Adelian, H. Mobarak, M.R. Hamblin, A. R. Aref, Tumor-derived exosomal non-coding RNAs as diagnostic biomarkers in cancer, Cell. Mol. Life Sci. 79 (11) (2022) 572, https://doi.org/10.1007/s00018-022-04552-3.

[6] J.X. Wei, K. Zhu, T.Y. Wang, T.S. Qi, Z.Y. Wang, J. Li, S.F. Zong, Y.P. Cui, Highly accurate profiling of exosome phenotypes using super-resolution tricolor fluorescence co-localization, ACS Nano 18 (14) (2024) 10206–10215, https://doi.org/10.1021/acsnano.4c00534.

[7] Z.X. Ye, M. Ma, Y.X. Chen, R.Y. Liu, Y. Zhang, P.Y. Ma, D.Q. Song, Dual-microRNA-controlled Electrochemiluminescence biosensor for breast Cancer diagnosis and supplemental identification of breast Cancer metastasis, Anal. Chem. 96 (8) (2024) 3636–3644, https://doi.org/10.1021/acs.analchem.3c05766.

[8] Z.X. Ye, M. Ma, Y.X. Chen, J.K. Yang, C. Zhao, Q.P. Diao, P.Y. Ma, D.Q. Song, Early diagnosis of triple-negative breast Cancer based on dual microRNA detection using a well-defined DNA crown-carbon dots structure as an Electrochemiluminescence sensing platform, Anal. Chem. 96 (45) (2024) 17984–17992, https://doi.org/10.1021/acs.analchem.4c02986.

[9] Z.W. Sun, J. Li, Y. Tong, H.C. Han, Y.F. Yang, C.X. Wang, H. Li, L.T. Du, Y.Y. Jiang, A ratiometric fluorescent biosensor based on self-fluorescent MOF and target-triggered rolling circle amplification for sensitive detection of exosome-derived miRNA, Anal. Chim. Acta 1221 (2022), https://doi.org/10.1016/j.aca.2022.340136.

[10] K. Boriachek, M. Umer, M.N. Islam, V. Gopalan, A.K. Lam, N.-T. Nguyen, M.J. A. Shiddiky, An amplification-free electrochemical detection of exosomal miRNA-21 in serum samples, Analyst 143 (7) (2018) 1662–1669, https://doi.org/10.1039/C7AN01843F.

[11] J.H. Lee, J.A. Kim, M.H. Kwon, J.Y. Kang, W.J. Rhee, In situ single step detection of exosome microRNA using molecular beacon, Biomaterials 54 (2015) 116–125, https://doi.org/10.1016/j.biomaterials.2015.03.014.

[12] E. Ban, E.J. Song, Considerations and suggestions for the reliable analysis of miRNA in plasma using qRT-PCR, Genes 13 (2) (2022) 328, https://doi.org/10.3390/genes13020328.

[13] A.E. Grigor'eva, N.S. Dyrkheeva, O.E. Bryzgunova, S.N. Tamkovich, B. P. Chelobanov, E.I. Ryabchikova, Contamination of exosome preparations, isolated from biological fluids, B Biochem. Moscow Suppl. Ser. B 11 (3) (2017) 265–271, https://doi.org/10.1134/S1990750817030040.

[14] Y.Y. Lu, Z.Z. Huang, Y.Z. Dong, D.Y. Yu, F. Jiang, Y. Han, Y.P. Chen, Magnetic Fe_3O_4@MOF@aptamer-mediated entropy-driven fluorescence biosensor for multiplexed and DNA extraction- and amplification-free detection of pathogenic bacteria, Chem. Eng. J. 499 (2024), https://doi.org/10.1016/j.cej.2024.155978.

[15] Y.Q. Wu, L. Chen, Y. Tong, C.S. Zhai, G.Y. Xiao, Y.P. Lv, L.T. Du, J. Li, P. Ren, Y. Y. Jiang, Magnetically-driven dual-channel fluorescent biosensor with aptamer logic gates for multiplexed Exosomal protein profiling and breast Cancer subtyping, Chem. Eng. J. 517 (2025), https://doi.org/10.1016/j.cej.2025.164324.

[16] J. Ma, K. Li, Z. Duan, X. Yang, G. Zhou, S. Ye, On-Chip isolation and reciprocal signal amplification detection of tumor-derived exosomes in dual-control microfluidic device, Anal. Chem. 97 (13) (2025) 7483–7489, https://doi.org/10.1021/acs.analchem.5c00426.

[17] C. Li, H. Wang, R. Wei, J. Ren, M. Zhou, C. Yan, L. Huang, An excellent colorimetric aptasensor integrating multifunctional SNAs and TdT-induced dual signal amplification for rapid sensitive detection of exosomes, Sens. Actuator B-Chem. 380 (2023) 133361, https://doi.org/10.1016/j.snb.2023.133361.

[18] W. Lu, Y. Chen, Z. Liu, W. Tang, Q. Feng, J. Sun, X. Jiang, Quantitative detection of MicroRNA in one step via next generation magnetic relaxation switch sensing, ACS Nano 10 (7) (2016) 6685–6692, https://doi.org/10.1021/acsnano.6b01903.

[19] Z. Lu, W. Ni, N. Liu, D. Jin, T. Li, K. Li, Y. Zhang, Q. Yao, G.-J. Zhang, CRISPR/Cas12a-based fluorescence biosensor for detection of exosomal miR-21 derived from lung cancer, Microchem. J. 187 (2023) 108370, https://doi.org/10.1016/j.microc.2022.108370.

[20] G. Zhang, L. Zhang, J. Tong, X. Zhao, J. Ren, CRISPR-Cas12a enhanced rolling circle amplification method for ultrasensitive miRNA detection, Microchem. J. 158 (2020) 105239, https://doi.org/10.1016/j.microc.2020.105239.

[21] H. Yan, Y. Wen, Z. Tian, N. Hart, S. Han, S.J. Hughes, Y. Zeng, A one-pot isothermal Cas12-based assay for the sensitive detection of microRNAs, Nat. Biomed. Eng. 7 (12) (2023) 1583–1601, https://doi.org/10.1038/s41551-023-01033-1.

[22] Z. Sun, J. Li, Y. Tong, Y. Yang, H. Li, C. Wang, L. Du, Y. Jiang, A ratiometric fluorescent biosensing strategy based on a composite nanoplatform and dual signal amplification for exosomal miRNA detection, Chem. Eng. J. 458 (2023) 141501, https://doi.org/10.1016/j.cej.2023.141501.

[23] Y. Tong, B. Guan, Z. Sun, X. Dong, Y. Chen, Y. Li, Y. Jiang, J. Li, Ratiometric fluorescent detection of exosomal piRNA-823 based on au NCs/UiO-66-NH2 and target-triggered rolling circle amplification, Talanta 257 (2023) 124307, https://doi.org/10.1016/j.talanta.2023.124307.

[24] Y. Xia, Z. Huang, T. Chen, L. Xu, G. Zhu, W. Chen, G. Chen, S. Wu, J. Lan, X. Lin, J. Chen, Sensitive fluorescent detection of exosomal microRNA based on enzymes-assisted dual-signal amplification, Biosens. Bioelectron. 209 (2022) 114259, https://doi.org/10.1016/j.bios.2022.114259.

[25] S.B. Seo, J. Lim, K. Kim, I. Maeng, H.W. Rho, H.Y. Son, E. Kim, E. Jang, T. Kang, J. Jung, S.J. Oh, Y.-M. Huh, E.-K. Lim, Nucleic acid amplification circuit-based hydrogel (NACH) assay for one-step detection of metastatic gastric Cancer-derived Exosomal miRNA, Adv. Sci. 11 (43) (2024) 2407621, https://doi.org/10.1002/advs.202407621.

[26] X. Zhao, X. Liu, T. Chen, H. Xie, S. Li, Y. Zhang, H. Zhang, Y. Cao, W. Du, X. Feng, X. Liu, Y. Li, P. Chen, Q. Li, B.-F. Liu, Fully integrated centrifugal microfluidics for rapid exosome isolation, Glycan Analysis, and Point-of-Care Diagnosis, ACS Nano 19 (9) (2025) 8948–8965, https://doi.org/10.1021/acsnano.4c16988.

[27] F. Song, C. Wang, C. Wang, J. Gao, H. Liu, Y. Zhang, L. Han, Enrichment-detection integrated exosome profiling biosensors promising for early diagnosis of Cancer, Anal. Chem. 93 (11) (2021) 4697–4706, https://doi.org/10.1021/acs.analchem.0c05245.

[28] H. Xu, B.-C. Ye, Integrated microfluidic platforms for tumor-derived exosome analysis, TrAC, Trends Anal. Chem. 158 (2023) 116860, https://doi.org/10.1016/j.trac.2022.116860.

[29] I. Helwa, J. Cai, M.D. Drewry, A. Zimmerman, M.B. Dinkins, M.L. Khaled, M. Seremwe, W.M. Dismuke, E. Bieberich, W.D. Stamer, M.W. Hamrick, Y. Liu, A comparative study of serum exosome isolation using differential ultracentrifugation and three commercial reagents, PLoS One 12 (1) (2017) e0170628, https://doi.org/10.1371/journal.pone.0170628.

[30] M. Faraldi, M. Gomarasca, V. Sansoni, S. Perego, G. Banfi, G. Lombardi, Normalization strategies differently affect circulating miRNA profile associated with the training status, Sci. Rep. 9 (1) (2019) 1584, https://doi.org/10.1038/s41598-019-38505-x.

[31] D. Sanz-Rubio, I. Martin-Burriel, A. Gil, P. Cubero, M. Forner, A. Khalyfa, J. M. Marin, Stability of circulating Exosomal miRNAs in healthy subjects, Sci. Rep. 8 (1) (2018) 10306, https://doi.org/10.1038/s41598-018-28748-5.

[32] C. Rajan, V.G.D. Roshan, I. Khan, V.G. Manasa, I. Himal, J. Kattoor, S. Thomas, P. Kondaiah, S. Kannan, MiRNA expression profiling and emergence of new prognostic signature for oral squamous cell carcinoma, Sci. Rep. 11 (1) (2021) 7298, https://doi.org/10.1038/s41598-021-86316-w.

[33] X. Qin, Y. Xiang, N. Li, B. Wei, Y. Chen, D. Fang, M. Fang, Q. Li, J. Liu, Y. Tang, X. Li, F. Yang, Simultaneous detection of cancerous exosomal miRNA-21 and PD-L1 with a sensitive dual-cycling nanoprobe, Biosens. Bioelectron. 216 (2022) 114636, https://doi.org/10.1016/j.bios.2022.114636.

[34] L. Luo, L. Wang, L. Zeng, Y. Wang, Y. Weng, Y. Liao, T. Chen, Y. Xia, J. Zhang, J. Chen, A ratiometric electrochemical DNA biosensor for detection of exosomal MicroRNA, Talanta 207 (2020) 120298, https://doi.org/10.1016/j.talanta.2019.120298.

[35] K. Li, J. Tu, Y. Zhang, D. Jin, T. Li, J. Li, W. Ni, M.-M. Xiao, Z.-Y. Zhang, G.-J. Zhang, Ultrasensitive detection of exosomal miRNA with PMO-graphene quantum dots-functionalized field-effect transistor biosensor, iScience 25 (7) (2022), https://doi.org/10.1016/j.isci.2022.104522.

[36] A. Asadirad, A. Khodadadi, A. Talaiezadeh, M. Shohan, M. Rashno, N. Joudaki, Evaluation of miRNA-21-5p and miRNA-10b-5p levels in serum-derived exosomes of breast cancer patients in different grades, Mol. Cell. Probes 64 (2022), https://doi.org/10.1016/j.mcp.2022.101831.

[37] H. Fang, J.P. Xie, M. Zhang, Z.W. Zhao, Y. Wan, Y.Q. Yao, miRNA-21 promotes proliferation and invasion of triple-negative breast cancer cells through targeting PTEN, Am. J. Transl. Res. 9 (3) (2017) 953–961.

[38] V. Kumar, M. Gautam, A. Chaudhary, B. Chaurasia, Impact of three miRNA signature as potential diagnostic marker for triple negative breast cancer patients, Sci. Rep. 13 (1) (2023), https://doi.org/10.1038/s41598-023-48896-7.

[39] M. Mathieu, N. Névo, M. Jouve, J.I. Valenzuela, M. Maurin, F.J. Verweij, R. Palmulli, D. Lankar, F. Dingli, D. Loew, E. Rubinstein, G. Boncompain, F. Perez, C. Théry, Specificities of exosome versus small ectosome secretion revealed by live intracellular tracking of CD63 and CD9, Nat. Commun. 12 (1) (2021) 4389, https://doi.org/10.1038/s41467-021-24384-2.

[40] J. Shi, Considering Exosomal miR-21 as a Biomarker for Cancer, J. Clin. Med 5 (4) (2016), https://doi.org/10.3390/jcm5040042.

[41] F.K. Yang, C. Tian, L.X. Zhou, T.Y. Guan, G.L. Chen, Y.Y. Zheng, Z.G. Cao, The value of urinary exosomal microRNA-21 in the early diagnosis and prognosis of bladder cancer, Kaohsiung J. Med. Sci. 40 (7) (2024) 660–670, https://doi.org/10.1002/kjm2.12845.

[42] M. Mathieu, N. Névo, M. Jouve, J.I. Valenzuela, M. Maurin, F.J. Verweij, R. Palmulli, D. Lankar, F. Dingli, D. Loew, E. Rubinstein, G. Boncompain, F. Perez, C. Théry, Specificities of exosome versus small ectosome secretion revealed by live intracellular tracking of CD63 and CD9, Nat. Commun. 12 (1) (2021) 4389, https://doi.org/10.1038/s41467-021-24384-2.

[43] C. Han, J. Yang, T. Yin, J. An, A. Qiao, Y. Cao, Y. Feng, H. Lu, Y. Wang, L. Yang, G. Qin, CD63-snorkel tagging for isolation of exosomes, Extracellular Vesicle 2 (2023) 100031, https://doi.org/10.1016/j.vesic.2023.100031.

[44] P. Yin, C. Huang, L. Zhang, Z. Li, C. Zhong, S. Kuang, C. Lei, Y. Huang, Z. Nie, Developing orthogonal fluorescent RNAs for photoactive dual-color imaging of RNAs in live cells, Angew. Chem. Int. Ed. 64 (14) (2025) e202424060, https://doi.org/10.1002/anie.202424060.

[45] S.J. Hurst, A.K. Lytton-Jean, C.A. Mirkin, Maximizing DNA loading on a range of gold nanoparticle sizes, Anal. Chem. 78 (24) (2006) 8313–8318, https://doi.org/10.1021/ac0613582.

[46] D.V. Sotnikov, N.A. Byzova, A.V. Zherdev, B.B. Dzantiev, Retention of activity by antibodies immobilized on gold nanoparticles of different sizes: Fluorometric method of determination and comparative evaluation, Nanomaterials (Basel) 11 (11) (2021), https://doi.org/10.3390/nano11113117.

[47] K. Tripathi, J.D. Driskell, Quantifying bound and active antibodies conjugated to gold nanoparticles: a comprehensive and robust approach to evaluate immobilization chemistry, ACS Omega 3 (7) (2018) 8253–8259, https://doi.org/10.1021/acsomega.8b00591.

[48] L. Luo, F. Dong, D. Li, X. Li, X. Li, Y. Fan, C. Qi, J. Luo, L. Li, B. Shen, Enhancing 3D DNA Walker-induced CRISPR/Cas12a Technology for Highly Sensitive Detection of ExomicroRNA associated with osteoporosis, ACS Sens. 9 (3) (2024) 1438–1446, https://doi.org/10.1021/acssensors.3c02533.

[49] D. Li, Q.-W. Li, H. Xiang, S.-S. Yuan, X.-P. Yang, A label-free activatable biosensor for in situ detection of exosomal microRNAs based on DNA-AgNCs and hairpin type nucleic acid probes, Anal. Methods 16 (9) (2024) 1357–1362, https://doi.org/10.1039/D3AY02268D.

[50] H. Kong, X. Chen, W. Lee, X. Xie, Y. Tao, M. Li, Dual-color fluorescence detection of tumor-derived extracellular vesicles using a specific and serum-stable membrane-fusion approach, Biosens. Bioelectron. 278 (2025) 117302, https://doi.org/10.1016/j.bios.2025.117302.

[51] X. Kang, C. Lei, J. Shi, X. Liu, W. Ren, C. Liu, A versatile CRISPR/Cas12a-based biosensing platform coupled with a target-protected transcription strategy, Biosens. Bioelectron. 219 (2023) 114801, https://doi.org/10.1016/j.bios.2022.114801.

[52] J.G. Han, Y.D. Jiang, C.H. Zhang, Y.M. Yang, D. Pang, Y.N. Song, G.Q. Zhang, A novel panel of serum miR-21/miR-155/miR-365 as a potential diagnostic biomarker for breast cancer, Ann. Surg. Treat. Res. 92 (2) (2017) 55–66, https://doi.org/10.4174/astr.2017.92.2.55.

[53] M. Li, Q. Li, Q. Yin, Y. Wang, J.M. Shang, L.H. Wang, Evaluation of color Doppler ultrasound combined with plasma miR-21 and miR-27a in the diagnosis of breast cancer, Clin. Transl. Oncol. 23 (4) (2021) 709–717, https://doi.org/10.1007/s12094-020-02501-9.

[54] W. Wang, X. Yuan, A. Xu, X. Zhu, Y. Zhan, S. Wang, M. Liu, Human cancer cells suppress behaviors of endothelial progenitor cells through miR-21 targeting IL6R, Microvasc. Res. 120 (2018) 21–28, https://doi.org/10.1016/j.mvr.2018.05.007.

[55] L.X. Yan, X.F. Huang, Q. Shao, M.Y. Huang, L. Deng, Q.L. Wu, Y.X. Zeng, J.Y. Shao, MicroRNA miR-21 overexpression in human breast cancer is associated with advanced clinical stage, lymph node metastasis and patient poor prognosis, RNA 14 (11) (2008) 2348–2360, https://doi.org/10.1261/rna.1034808.

[56] S. Khalighfard, A.M. Alizadeh, S. Irani, R. Omranipour, Plasma miR-21, miR-155, miR-10b, and let-7a as the potential biomarkers for the monitoring of breast cancer patients, Sci. Rep. 8 (1) (2018) 17981, https://doi.org/10.1038/s41598-018-36321-3.

[57] M.-J. Lee, J.-H. Shin, S.-H. Jung, J.-W. Choi, H.R. Ahn, J.-H. Choi, B.-K. Oh, Hourglass-inspired total analysis system for the sensitive colorimetric detection of exosomal miRNA using the CRISPR-Cas12a system with isothermal amplification, Chem. Eng. J. 512 (2025) 162729, https://doi.org/10.1016/j.cej.2025.162729.